

AOne-year Continuous Observations of Near-Surface Atmospheric Water Vapor Stable Isotopes at Matara, Sri Lanka

3 Yuqing Wu ^{1,2}, Jing Gao ^{1,3,*}, Aibin Zhao ¹, Xiaowei Niu ¹, Yigang Liu ¹,
4 ², Disna Ratnasekera ^{4,5}, Tilak Priyadarshana Gamage ⁶, Amarasinghe
5 Hewage Ruwan Samantha ⁶

6 *1 State Key Laboratory of Tibetan Plateau Earth System, Resources and Environment,*
7 *Institute of Tibetan Plateau Research, Chinese Academy of Sciences, Beijing 100101,*
8 *China*

9 2 University of the Chinese Academy of Sciences, Beijing, 100049, China

10 *3 Lanzhou University, Lanzhou 733000, China*

11 *4 China-Sri Lanka Joint Center for Education & Research, Guangzhou 510301, China*

12 *5 Department of Agricultural Biology, Faculty of Agriculture, University of Ruhuna,*
13 *Matara 81000, Sri Lanka*

14 6 Faculty of Fisheries and Marine Sciences & Technology, University of Ruhuna,
15 Matara 81000, Sri Lanka

16 *Corresponding *to author*: Jing Gao (gaojing@itpcas.ac.cn)

18 **Abstract:**

Atmospheric water vapor stable isotopes are crucial for understanding hydrological cycle processes under climate change. This study presents [the results from](#) a year-long in-situ monitoring of atmospheric water vapor stable isotopes ($\delta^{18}\text{O}$, δD) at Matara, Sri Lanka, from March 2020 to February 2021 to assess how oceanic sources and moisture transport influence coastal atmospheric moisture isotopic composition. We identified clear seasonal patterns in the isotopic composition, with $\delta^{18}\text{O}$, δD , and d-excess showing substantial variation between the southwest and northeast monsoon periods. The primary moisture sources were the Arabian Sea and the Indian Ocean during the southwest monsoon (May to September), characterized by [lower amplitude](#) values of depleted $\delta^{18}\text{O}$ from $(-20.4\text{\textperthousand})$ to $(-9.1\text{\textperthousand})$. During the northeast monsoon

29 ~~dominated period~~, the northern Bay of Bengal, the Indian subcontinent, and Southeast
30 Asia were primary moisture sources, ~~resulting displayed enriched higher amplitude~~
31 ~~values of~~ $\delta^{18}\text{O}$ (-23.9‰ to -7.5‰) and higher d-excess values (up to 25 ‰). The study
32 also identified significant influences of sea surface temperature and sea surface relative
33 humidity, on the isotopic composition of water vapor. Additionally, ~~we could use~~
34 outgoing longwave radiation (OLR) ~~is a significant index used~~ to gauge the intensity of
35 convective activity. Lower OLR values, indicative of stronger and deeper convection,
36 were associated with ~~air masses that were more depleted in~~ $\delta^{18}\text{O}$ ~~in air masses~~. These
37 findings ~~facilitate a better help to improve the~~ understanding of ~~influences of how~~ the
38 monsoon and local meteorological conditions ~~affect on~~ water vapor isotope
39 ~~compositions~~ in tropical region. ~~Furthermore, we and provide present a~~ new dataset
40 ~~on that should enable improved enhancing~~ water vapor isotopic modeling ~~or and~~
41 ~~projections of~~ atmospheric processes ~~projection~~ in coastal regions.

42 **Keywords:** Indian Summer Monsoon, Water Vapor Isotopes, Sea Surface Condition,
43 Convective Activity, Sri Lanka

44

45 **Short Summary**

46 ~~This study mMonitor eding of~~ atmospheric water vapor isotopes for ~~a one~~ year at
47 Matara, Sri Lanka, ~~yielded It found~~ clear seasonal variations in $\delta^{18}\text{O}$, δD , and d-excess.
48 ~~There The results~~ showed ~~lower amplitudes of depleted~~ $\delta^{18}\text{O}$ during the southwest
49 monsoon, ~~while had enriched and higher amplitudes of~~ $\delta^{18}\text{O}$ and higher d-excess during
50 the northeast monsoon. Sea surface ~~evaporation condition~~ and regional convective
51 activity significantly influenced ~~the~~ isotopic compositions, ~~. Overall, our results~~
52 ~~facilitate an improving improved~~ understanding of ~~the impacts of~~ monsoon and local
53 meteorological condition ~~impacts~~ on tropical water vapor ~~isotopic composition~~.

54

55 **1 Introduction**

56 The Indian Summer Monsoon (ISM), occurring from June to September, is a
57 pivotal component of the Asian climate system, serving as the primary transport of

58 moisture from the Indian Ocean to the Indian subcontinent and the Tibetan Plateau (TP).
59 Monsoonal precipitation plays a crucial role in agriculture and water resources
60 availability, affecting the welfare of over 1.9 billion people in surrounding countries
61 (Webster et al., 1998; Goswami et al., 2016). The Tibetan climate and hydrology are
62 profoundly influenced by the ISM, as it contributes significantly to the regional water
63 cycle by delivering substantial rainfall during the summer months. This rainfall is
64 essential for maintaining the glaciers and permafrost in the TP, which area key sources
65 of waterwater catchment area for many of Asia's largest rivers (Bookhagen and Burbank,
66 2010). The ISM's intensity and variability can lead to significant fluctuations in water
67 availability, affecting both agriculture and hydropower generation in the region (Singh
68 and Bengtsson, 2004; Gao et al., 2014). Furthermore, the interaction between the ISM
69 and the TP's topography creates unique climatic conditions that influence weather
70 patterns and extreme events in the region (Liu and Chen, 2000).

71 The seasonal precipitation and its origins over the TP are inextricably linked to
72 the dynamics of the ISM (Dai et al., 2021). Previous studies have provided evidence
73 that isotopic records derived from precipitation over the TP offer insights into the
74 climatic fluctuations and distinct moisture attributes associated with the ISM (Gao et
75 al., 2013; Guo et al., 2017). The summer monsoon brings significant moisture from the
76 Indian Ocean, leading to substantial rainfall over the TP primarily during the monsoon
77 months during of June-September (Yao et al., 2012). This seasonal influx of moisture
78 is critical for maintaining the regional hydrological balance and supporting the
79 ecosystems. Furthermore, the ISM's intensity and variability significantly influence the
80 interannual and decadal precipitation patterns over the TP, affecting the overall water
81 availability and climatic stability of the region (Kaushal et al., 2018).

82 The stable isotopic composition of river water (Bershaw et al., 2012; Li and
83 Garzjone, 2017), precipitation (Rahul et al., 2016a; Cai et al., 2017), and water vapor
84 (Risi et al., 2008; Steen-Larsen et al., 2013b; Rahul et al., 2016b; Lekshmy et al., 2022)
85 serves as a valuable tool for understanding identifying the origins and understanding
86 transmission processes of atmospheric water vapor. Fractionation occurs during various

phase transitions, such as sea surface evaporation, condensation beneath clouds, re-evaporation of raindrops, and diffusive exchanges between water vapor and raindrops (Stewart, 1975; Benetti et al., 2018; Graf et al., 2019). The occurrence of fractionation unveils investigable spatiotemporal distribution patterns in the water isotopic composition, encompassing water vapor and precipitation. In this context, D_{deuterium excess} (d-excess = δD – 8 × δ¹⁸O) is a useful parameter for studying kinetic fractionation effects (Dansgaard, 1964). Recent studies have significantly enhanced our understanding of isotopic signals in convection regions, illuminating elucidating the complex interactions between moisture processes and isotopic compositions in tropical deep convection. Around Barbados, during In the winter trades near Barbados winds, vertical transport and large-scale circulations have been identified as primary drivers of isotopic variability at the cloud base, acting over timescales from hours to days (Bailey et al., 2023; Villiger and Aemisegger, 2024). Investigations into water vapor isotopes in the West African troposphere reveal that both convection and mixing emphasize highlight the important role of played by large-scale atmospheric circulation processes in the variations of water vapor isotopes (Diekmann et al., 2021; de Vries et al., 2022). The precise mechanisms by which convective activity reduces the amount of lowers stable isotopes values of in water vapor and precipitation are still under debate. Some researchers have emphasized the significance of condensation levels (Cai and Tian, 2016; Permana et al., 2016; Thompson et al., 2017), while others suggested point to raindrop re-evaporation and raindrop-vapor isotope exchanges during strong convection as crucial factors (Galewsky et al., 2016). Additionally, unsaturated or mesoscale descending airflows that transport vapor depleted in heavy isotopes to the lower atmosphere also contribute to lower isotope values (Risi et al., 2008; Kurita, 2013). The influence of these processes varies with the intensity of convective activity. These studies provide valuable insights. However, there is a paucity of study on the Indian Ocean, particularly in relation to Sri Lanka. This gap underscores the need to explore isotopic signals in this region, with reference to established findings by Risi et al. (2008) and other seminal works. Comparison with the above results, recent studies

116 on water stable isotopes in the South Indian Ocean and South Asian region have
117 uncovered connections between local processes and atmospheric circulation, shedding
118 light on sea surface dynamics (Midhun et al., 2013; Rahul et al., 2016b; Bonne et al.,
119 2019). Fractionation occurs during various phase transitions, such as sea surface
120 evaporation, condensation beneath clouds, re-evaporation of raindrops, and diffusive
121 exchange between water vapor and raindrops (Stewart, 1975; Benetti et al., 2018; Graf
122 et al., 2019). The occurrence of fractionation unveils investigable spatiotemporal
123 distribution patterns in the water isotopic composition, encompassing water vapor and
124 precipitation. Deuterium excess (d excess = $\delta D - 8 \times \delta^{18}\text{O}$) is a useful parameter for
125 studying kinetic fractionation effects (Dansgaard, 1964). Compared to other water
126 stable isotopes, such as those found in precipitation and surface water, the monitoring
127 of atmospheric water vapor isotopes is not limited by season, weather, or location
128 (Angert et al., 2008). This capability for full time and full space observation allows for
129 the avoidance of information loss during sampling, thereby providing a more
130 comprehensive, continuous insight into the evolving processes of atmospheric water
131 vapor transport from diverse sources and a thorough understanding of isotope
132 transformation processes within the water cycle.

133 Evaporation at the ocean surface constitutes a significant component of the global
134 water cycle and is pivotal ~~in~~ for the accurately modeling of climate change. ~~The primary~~
135 ~~objective of~~ ~~Typically~~, research on water vapor stable isotopes in the marine boundary
136 layer aims to elucidate the processes ~~associated with evaporation isotopes as well as~~ ~~nd~~
137 influencing factors ~~of evaporation isotopes~~ (Craig and Gordon, 1965). The d -excess of
138 evaporated water vapor is ~~predominantly mainly~~ impacted by dynamic fractionation
139 associated with sea surface temperature (SST), the relative humidity ~~of~~ ~~above~~ the sea-
140 surface ~~air~~ (RH_{SST}, calculated relative to the saturation vapor pressure at SST), and wind
141 speed (rough or smooth) (Benetti et al., 2015; Benetti et al., 2018). Investigations into
142 the water vapor stable isotopic composition within the marine boundary layer have been
143 principally ~~concentrated around focused on~~ regions ~~such as including a large part of~~ the
144 North Atlantic Ocean (such as e.g., Greenland, Iceland, Bermuda) (Steen-Larsen et al.,

145 2013a; Bonne et al., 2014; Benetti et al., 2018; Bonne et al., 2019), Bay of Bengal (BoB)
146 (Lekshmy et al., 2022), and ~~the ocean throughout the Atlantic and~~ Arctic Oceans (Kurita,
147 2011). ~~These Several~~ studies ~~have validated~~~~could confirm~~ the ~~existence of a~~ negative
148 relationship between d-excess and RH_{SST} (Uemura et al., 2008; Steen-Larsen et al.,
149 ~~with suggesting that~~ wind speed and SST exerting a limited influence on this
150 correlation (Benetti et al., 2015). Observations from the North Atlantic ~~bolster support~~
151 this theory (Benetti et al., 2014). In addition, ~~it also highlights the studies found~~
152 significant variations in d-excess values ~~in vapor that originated at~~ ~~from~~ different
153 moisture sources (Kurita, 2011; Steen-Larsen et al., 2013b; Delattre et al., 2015).
154 Subsequently, Benetti et al. (2015) introduced a multi-layer mixing model, which is
155 expected to ~~advance improve~~ the accuracy of d-excess and water vapor isotope
156 simulations. Due to the impact of dynamic fractionation on sea surface ~~water~~
157 evaporation, some studies have focused on simulating observed d-excess under the
158 closure assumption (Bonne et al., 2019). ~~Furthermore, researchers Others~~ have used
159 isotope atmospheric circulation models to assess mixing and transport processes within
160 the marine boundary layer (Benetti et al., 2015). Owing to the minor influence of
161 transport-induced fractionation, d-excess ~~of in~~ the marine boundary layer is
162 ~~conventionally typically~~ employed to deduce moisture sources (Benetti et al., 2018).

163 Amidst the ~~current~~ backdrop of global climate change, observing stable isotopes
164 in atmospheric water vapor is vital for monitoring and ~~comprehending understanding~~
165 climate shifts in ~~tropical~~ low-latitude areas (Rahul et al., 2016b). Such research is
166 instrumental ~~in for~~ providing a deeper understanding of near-surface water vapor
167 dynamics, pinpointing vapor sources and transport routes, and differentiating ~~the~~
168 ~~between different~~ contributions of atmospheric water vapor to the water cycle.

169 ~~Positioned Located~~ in the northern ~~expanse of the~~ Indian Ocean, Sri Lanka
170 ~~experiences pronounced impacts from both~~~~is impacted by both~~ the southwest monsoon
171 and ~~the~~ northeast monsoons (Fig. 1a, b) ~~and~~. ~~It emerges has been identified~~ as an
172 ~~important prominent~~ origin region for monsoonal water vapor ~~in over~~ the TP. ~~However,~~
173 ~~only few studies have focused on the Indian Ocean, and even fewer on the area around~~

174 Sri Lanka. This knowledge gap underscores the need to explore isotopic signals in this
175 region and place them into their appropriate context, e.g., with findings by Risi et al.
176 (2008). For instance, more recent studies on water stable isotopes in the South Indian
177 Ocean and South Asian region have uncovered connections between local processes
178 and large-scale atmospheric circulation, shedding light on sea-surface dynamics
179 (Midhun et al., 2013; Rahul et al., 2016b; Bonne et al., 2019). Unlike, in precipitation
180 and surface water, in atmospheric water vapor stable isotopes can be monitored
181 continuously regardless of season, weather, or location (Angert et al., 2008). This
182 potentially full temporal and spatial coverage allows for a more comprehensive and
183 continuous monitoring of atmospheric water vapor dynamics and transport, which
184 should in turn facilitate a deeper understanding of isotope transformation processes
185 within the water cycle. Therefore, investigating the dynamics and variations of near-
186 surface atmospheric water vapor stable isotopes at coastal stations, is not only pivotal
187 for monitoring identifying monsoonal water vapor source regions, but will facilitate
188 a better enhances our understanding of precipitation processes in over the Indian Ocean.
189 Oceanic evaporation serves as the inaugural stage in therepresents the first of many
190 phase transitions that occur during the global water cycle phase transition. The primary
191 objective of researching water vapor stable isotopes is to comprehend the processes and
192 controlling factors of water isotopic variations.

193 In this study, we conducted continuous observations of present the results from
194 continuous observations of near-surface atmospheric water vapor stable isotopes in
195 Matara, Sri Lanka, collected from March 1, 2020, to February 28, 2021. Our goal is We
196 analyze the observational data to gain a better understanding of the main variations in
197 moisture sources and main transmission processes in tropical coastal regions, and
198 to Furthermore, we explore how sea surface processes, convective activity, and local
199 meteorological factors affect near-surface atmospheric water vapor stable isotopes at a
200 coastal station, across daily, monthly, and seasonal (monsoonal) time scales. Section 2
201 gives an overview of the study site, covering and presents the meteorological and water
202 vapor observations, calibration protocols, and analysis methods. In Section 3, we

203 illustrate the variability of isotopic and meteorological parameters, analyze moisture
204 sources, assess the impact of sea surface processes on water vapor isotopes, and explore
205 the relationship between water vapor isotopes, convective activity, and local
206 meteorological observations.

207

208 **2 Study Site, Data, and methodsMethods**

209 **2.1 Study site-Site and meteorological-Meteorological data-Data**

210 Sri Lanka (located between approximately 6°N to 10°N and 79° to 82°E),) is the
211 southernmost country of on the Indian subcontinent,-is and a key region for identifying
212 the moisture source of the south Asian summer monsoon (Ravisankar et al., 2015).
213 Features-Featuring a tropical climate, Sri Lanka experiences four distinct monsoon
214 seasons annually: the northeast monsoon from December to February, the first inter-
215 monsoon from March to April, the southwest monsoon from May to September, and the
216 second inter-monsoon from October to November (Malmgren et al., 2003; Jayasena et
217 al., 2008). For the analyses, we combined the first and second inter-monsoon periods
218 into a single “non-monsoon period”. Most of the precipitation in Sri Lanka comes from
219 the southwest and northeast monsoon systems, accounting for over 7078% of the total
220 annual precipitation (Fig. 1c). Precipitation formation in Sri Lanka primarily relies on
221 organized convection associated with the Intertropical Convergence Zone (ITCZ) and
222 low-pressure systems (Gadgil, 2003), and while the associated moisture that derives
223 precipitation is primarily derived from originate in the Indian Ocean and BoB (Bandara
224 et al., 2022). The southwest monsoon transports moisture from the Indian Ocean to
225 southwestern Sri Lanka (Fig. 1a,b), where it leading leads to increased rainfall in the
226 southwestern region of Sri Lanka compared to the northeast (Bavadekar and Mooley,
227 1981). SimilarlyIn contrast, the northeast monsoon carries water vapor from the BoB
228 to the northern and northeastern of Sri Lanka (Fig. 1b), where it produces
229 disproportionately high amounts of rainfall compared to the southwest of the country
230 (Dhar and Rakhecha, 1983; Wang, 2006).

231 An automated weather station (AWS) was installed at the University of Ruhuna,

232 Matara (located at 5.94°N, 80.57°E) on the southern coast of Sri Lanka (Fig. 1d). It
 233 collected real-time meteorological observations, including air temperature,
 234 precipitation, relative humidity, vapor air pressure, wind speed, and wind direction,
 235 from March 1, 2020, to February 28, 2021. Based on the measured air temperature,
 236 relative humidity, and air pressure, we can compute the lifting condensation level (LCL)
 237 using (Dirmeyer et al., 2013):

$$\log E = -7.90298 \times \left(\frac{373.16}{T_{\text{obs. air}}} - 1 \right) + 5.02808 \times \log 10 \left(\frac{373.16}{T_{\text{obs. air}}} \right) - 1.3816 \times 10^{-7} \times \left(10^{\left(11.344 \times \left(1 - \frac{T_{\text{obs. air}}}{373.16} \right) - 1 \right)} + 8.1328 \times 10^{-3} \times \left(10^{\left(-3.49149 \times \left(\frac{373.16}{T_{\text{obs. air}}} - 1 \right) \right)} - 1 \right) + \log 10(1013.246) \right) \quad (1)$$

$$E_{\text{true}} = E \times RH \quad (2)$$

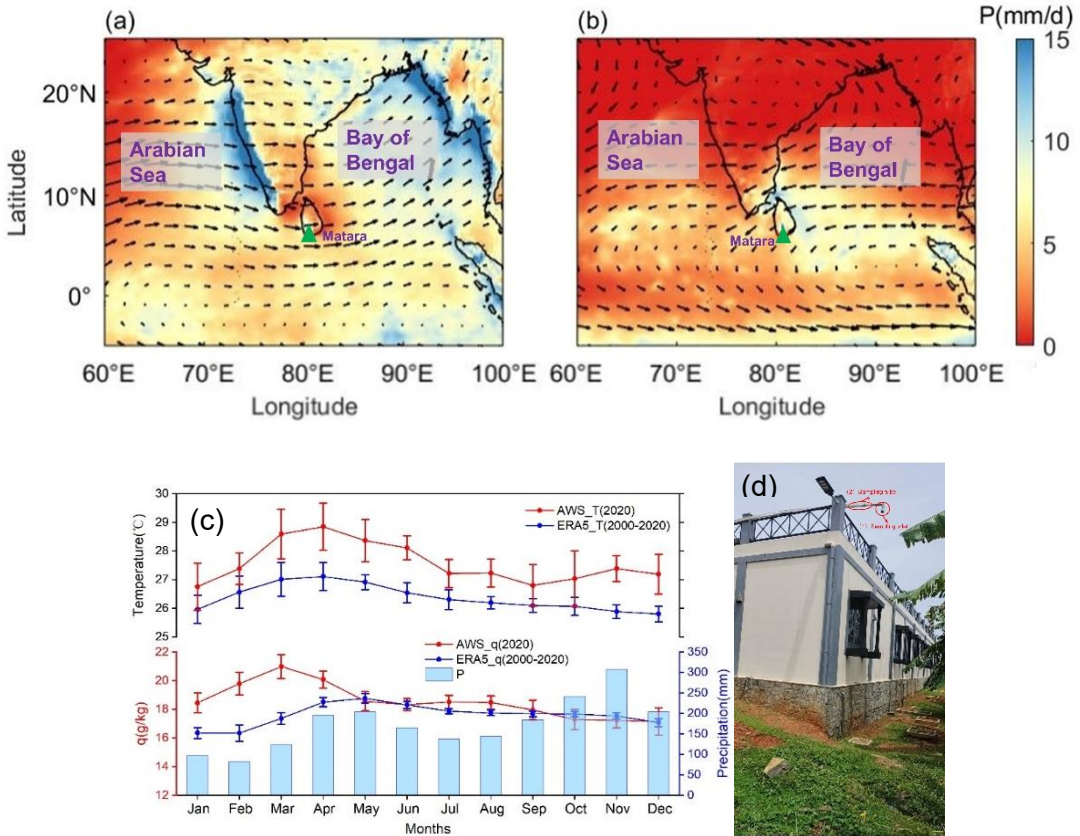
$$W = 0.622 \times \frac{E_{\text{true}}}{P - E_{\text{true}}} \quad (3)$$

$$T_{\text{dew}} = \frac{B}{\log \left(\frac{A \times 0.622}{W \times P} \right)} \quad (4)$$

$$LCL = 125 \times (T_{\text{obs. air}} - T_{\text{dew}}) \quad (5)$$

238 where E is the saturated vapor pressure, obtained from the improved Goff-Gratch
 239 formula (Goff and Gratch, 1946); E_{true} is the actual water vapor pressure; RH and W
 240 are relative humidity and mixing ratio, respectively; $T_{\text{obs. air}}$ and T_{dew} are the air
 241 temperature measured directly by the AWS and dew point temperature, respectively; P
 242 is the air pressure. The constants A and B have values of 2.53×10^8 kPa and $5.42 \times$
 243 10^3 , respectively.

244 Meteorological data are compared with water vapor isotopic data measured during
 245 the same period. ~~The annual average precipitation is 2085 mm, and the annual average~~
 246 ~~air temperature is 27.58°C~~ ~~b~~Based on the European Centre for Medium-Range Weather
 247 Forecasts (ECMWF, <https://cds.climate.copernicus.eu/eu/>) reanalysis dataset (ERA5),
 248 ~~the annual average precipitation and air temperature for the period~~ from 2000 to 2020
 249 is 2085 mm and 27.6 °C, respectively (Fig. 1c) (Hersbach et al., 2020).



252 **Figure 1: Mean wind vectors (arrows) at 850 hPa during the (a) 2020 southwest monsoon and**
 253 **(b) 2020/2021 northeast monsoon seasons, along with mean precipitation (P, light-blue**
 254 **rectangle base colors) from ERA5 averaged for the same period for the same. (c) Monthly mean**
 255 **temperature and specific humidity (q) obtained from an-the automated weather station at**
 256 **Matara station- (January and February are from 2021 while March – December from 2020),**
 257 **(averaged for the years 2020-2021), as well aswith monthly average temperature, specific**
 258 **humidity, and precipitation (from ERA5; (averaged for the years 2000-2020) plotted for**
 259 **comparison. (d) Photograph of the top floor platform roof-mounted weather station at the**
 260 **University of Ruhuna-where the system is installed, Sri Lanka.**

261 In this study, we used daily and monthly averages of outgoing longwave radiation
 262 (OLR, <https://www.esrl.noaa.gov/psd/data/gridded/data.ncep.reanalysis.pressure.html>)
 263 to quantify the convective activity. In addition, we used hourly data of 2m air
 264 temperature, 2m dew temperature, air pressure, precipitation, evaporation, SST,
 265 atmospheric boundary layer height (BLH), wind speed, and wind direction, obtained
 266 from ERA5 for years 2000 to 2021, with a spatial resolution of $0.25^\circ \times 0.25^\circ$ and a

267 temporal resolution of hourlyone hour. Studies have shown that ERA5 temperature,
268 precipitation and other data provide good representations of the Matara equatorial
269 climate and can be used in lieu of missing observational data (Bandara et al., 2022).

270 Due to weather conditions and instrument trouble, specific humidity measured by the
271 isotopic measurement instrument and computed by the AWS are missing from March,
272 2020 to April, 2020. Therefore, we chose to present both variables obtained from ERA5
273 as they complement each other, providing a clearer picture of humidity changes at
274 Matara station.

275 For the atmosphere above open sea regions, RH_{SST} is obtained by the following
276 formula using (Bonne et al., 2019):

$$RH_{SST} = RH_{2m\ air} \times \frac{q_{sat}(T_{2m\ air})}{q_{sat}(SST)} \quad (46)$$

277 where RH_{2m air} is the relative humidity at2m above the ocean surface, q_{sat}(T_{2m air}) is
278 the specific humidity at a saturated condition for a given 2m air temperature, and
279 q_{sat}(SST) is calculated for seawater atwith a salinity of 35 Practicalpractical salinity
280 units (PSU) (Curry and Webster, 1999).

281 The calculation formulas for to calculate air saturation specific humidity q_{sat}(T_{air})
282 and sea surface saturation specific humidity q_{sat}(SST) (sea surface salinity of 35 PSU)
283 are:

$$q_{sat}(T_{air}) = \frac{0.622 \times E}{P} \quad (27)$$

$$q_{sat}(SST) \quad (\text{sea surface salinity of 35 PSU}) = 0.98 \times \\ q_s \quad (\text{sea surface salinity of 35 PSU}) \quad (38)$$

284 among them, the calculation method of q_s (sea surface salinity of 35 PSU) represents
285 specific humidity and is calculated in the same way as that of q_{sat}(T_{air}). E is the
286 saturated water vapor pressure, obtained from the improved Goff-Gratch formula (Goff
287 and Gratch, 1946). P is atmospheric pressure, and the sea surface pressure is

288 taken as a fixed value of 1013.25 hPa calculated using atmospheric pressure for
289 calculation.

290 **2.2 In-situ Observation of Atmospheric Water Vapor Isotopic 291 Compositions**

292 At the Matara site, near-surface atmospheric water vapor isotope measurements
293 aim to establish a continuous, high resolution dataset with one second time intervals.
294 This study utilizes a Water Vapor Isotope Analyzer (manufactured by Los Gatos
295 Research (LGR) Inc.) in conjunction an LGR Water Vapor Isotope Standard Source
296 (WVISS model). The LGR instrument leverages Off-Axis Integrated Cavity Output
297 Spectroscopy (Off-Axis ICOS), a laser spectroscopic technique. This method integrates
298 a laser resonance cavity with a gas measurement chamber, where the laser oscillates
299 repeatedly between mirrors at the ends of the cavity. Only a small fraction of the laser
300 reaches the detector after traversing the sample gas thousands of times, effectively
301 increasing the chamber's thickness and significantly enhancing the water vapor
302 absorption signal. This allows for the detection of low concentrations of D and ^{18}O in
303 water vapor (Liu et al., 2015). Compared to traditional methods, this spectroscopic
304 technique offers three advantages: it is compact and portable, enabling real-time field
305 monitoring; it can simultaneously measure $\delta^{18}\text{O}$ and δD ; and it has lower measurement
306 costs and requires less operator expertise, facilitating broader adoption.

307 The analytical system for measuring atmospheric water vapor stable isotopes in
308 Sri Lanka situated approximately 100 meters from the sea (5.94° N, 80.57° E, 10
309 meters), consists of four primary components: (1) Sampling inlet it positioned
310 approximately 5 meters above the ground, atop the office building of the China Sri
311 Lanka Joint Center for Education and Research at the University of Ruhuna (see Figure
312 1d). The inlet is equipped with a stainless steel mesh to prevent the interference of
313 insects and directed downward to avoid direct rain splashes. (2) A 1/4 inch outer
314 diameter stainless steel tubing was used. The sampling tube is insulated with heating
315 tape and 2 cm thick insulation pipe to maintain warmth. (3) XX generates a constant
316 water vapor flow with known isotopic composition at different humidity levels. (4)

317 Water vapor isotope analyzer. In this study, the measurement precision of $\delta^{18}\text{O}$ and δD
318 reaches 0.25‰ and 0.5‰, respectively, at a concentration of 2500 ppmv. This setup
319 minimizes external influences and maintains the integrity of the sampled water vapor.

320 The water vapor analytical system is located adjacent to the AWS, ensuring a high
321 level of synchrony between the water vapor stable isotope data and meteorological
322 measurements. We define wind directions ranging from 60° to 330°N are defined as
323 reflecting the ocean region, while those from 330° to 60°N reflect the land (Figure 1).

324 The δ notation, expressed in per mil (‰), is used to represent the atmospheric
325 water vapor stable isotopes, using the following equations:

$$R_{\text{sample}} = \frac{\frac{1}{2}\text{H}_2^{18}\text{O}}{\frac{1}{2}\text{H}_2^{16}\text{O}} \quad (4)$$

$$R_{\text{D}} = \frac{\frac{1}{2}\text{D}}{\frac{1}{2}\text{H}_2^{16}\text{O}} \quad (5)$$

$$\delta_{\text{sample}} = \left(\frac{R_{\text{sample}}}{R_{\text{VSMOW}}} - 1 \right) \times 1000\% \quad (6)$$

326 Here, δ_{sample} represents either $\delta^{18}\text{O}$ or δD , indicating the ^{18}O or D isotope ratio
327 relative to Vienna Standard Mean Ocean Water (VSMOW) in the sample. R_{sample} and
328 R_{VSMOW} are the ^{18}O or D sample and VSMOW isotope ratios.

329 2.2 In-situ Observations of Atmospheric Water Vapor Isotopic 330 Composition

331 Near-surface atmospheric water vapor isotope measurements at Matara were
332 collected using a sampling frequency of 1Hz with the instrument located approximately
333 5m from the AWS. We used a Water Vapor Isotope Analyzer (Los Gatos Research (LGR)
334 Inc.) in conjunction with an LGR Water Vapor Isotope Standard Source (WVISS) model.
335 The LGR instrument employs a mirrored sampling chamber in which the laser traverses
336 the sample volume thousands of times, effectively amplifying the water vapor
337 absorption signal which facilitates the detection of low concentrations of D and ^{18}O
338 (Liu et al., 2015). Compared to traditional methods, this spectroscopic technique offers
339 three advantages: (i) it is compact and portable, enabling real-time field monitoring; (ii)

340 it can simultaneously measure $\delta^{18}\text{O}$ and δD ; and (iii) it has lower measurement costs
341 and requires less operator expertise.

342 The instrumental setup was situated approximately 100 m from the sea shore (5.94°
343 N, 80.57° E, 10 meters), and consisted of four primary components: (1) A sampling
344 inlet, positioned approximately 5 m above the ground (Fig. 1d), equipped with a
345 stainless-steel mesh to prevent interference from insects and facing downward to avoid
346 direct impacts from rain. (2) A 1/4-inch outer diameter stainless steel sampling tube,
347 insulated with heating tape and a 2-cm thick pipe for thermal insulation. (3) The
348 calibration unit to generate a constant flow of water vapor with known isotopic
349 composition and at different humidity levels. (4) A water vapor isotope analyzer,
350 delivering a measurement precision for $\delta^{18}\text{O}$ and δD of 0.25‰ and 0.5‰, respectively
351 (a concentration of 2500 ppmv). This setup has been designed to minimize external
352 influences and maintain the integrity of the sampled water vapor.

353 The spatial proximity between the water vapor analyzer and AWS ensures a high
354 level of synchronicity between the isotope and meteorological measurements. We
355 define wind directions from 60° to 330°N as oceanic, while those from 330° to 60°N as
356 terrestrial winds (Fig. 1a, b).

357 Atmospheric water vapor stable isotopes are expressed using the δ notation (in per
358 mil, ‰), using the following equations:

$$R_{^{18}\text{O}} = \frac{^{18}\text{O}}{^{16}\text{O}} \quad (9)$$

$$R_{\text{D}} = \frac{\text{D}}{\text{H}} \quad (10)$$

$$\delta_{\text{sample}} = \left(\frac{R_{\text{sample}}}{R_{\text{VSMOW}}} - 1 \right) \times 1000\% \quad (11)$$

359 Here, δ_{sample} represents either $\delta^{18}\text{O}$ or δD (^{18}O or D isotope ratio) relative to Vienna
360 Standard Mean Ocean Water (VSMOW). R_{sample} and R_{VSMOW} are the ^{18}O or D and
361 VSMOW isotope ratios, respectively.

362 2.3 Calibration Protocol

363 In this study, we adhere to the calibration protocol proposed by Steen-Larsen et al.

364 (2013b). Briefly, the instrument calibration and data processing consist of three major
365 steps: (1) ~~instrumental~~ humidity-isotope response calibration, (2) ~~Vienna Standard~~
366 ~~Mean Ocean Water~~SMOW - Standard Light Antarctic Precipitation (VSMOW-SLAP)
367 calibration, and (3) drift correction (~~refer to see~~ Text S1 in the Supporting Information).

368 The water vapor concentration can influence the measured water vapor isotopic
369 composition, known as concentration- or humidity-isotope dependency
370 characterization. By ~~introducing adding~~ a constant stream of water vapor ~~concentration~~
371 with ~~a~~ known isotopic composition at different humidity levels, we can establish the
372 humidity-isotope response function (Sturm and Knohl, 2010; Aemisegger et al., 2012).
373 As this function ~~may can~~ vary over time, ~~the humidity-isotope response its~~ calibration
374 was repeated monthly, using two standard samples ~~with well of~~ known isotopic
375 compositions measured at humidity levels ranging from 16,000 to 38,000 ppmv at
376 intervals of 1000 ppmv, ~~to establish a correction function~~. Each ~~level was measurement~~
377 ~~measured level was conducted~~ for ~~a minimum of at least~~ 25 minutes using the LGR
378 WVISS. Our results are referenced to a humidity level of 20,000 ppmv. We compared
379 our measurements to the international VSMOW-SLAP scale, assuming a linear drift
380 between calibration points.

381 ~~All measurements are subject to To compensate for~~ instrumental ~~internal~~ drift,
382 ~~necessitating correction through a specific drift correction procedure. To compensate~~
383 ~~for this drift, we the LGR WVISS generates water vapor from a drift standard bottle is~~
384 ~~measured the water vapor from a drift-standard bottle~~ for 25 minutes after each 12 hours
385 ~~performed an of~~ ambient air measurements. Furthermore, ~~we tested for instrument drift~~
386 ~~as part of the this drift standard water is sampled at each~~ routine ~~instrument~~ maintenance
387 ~~interval., assuming a linear drift between each drift-standard measurement.~~ Laboratory
388 analyses of liquid isotopes have confirmed the stability of its isotopic composition over
389 time. ~~A linear drift is assumed between each drift standard measurement.~~

390 **2.4 Rayleigh Distillation Model and MBL-Mixing Model**

391 The Rayleigh distillation model is employed to quantify isotopic variations during
392 phase changes (Dansgaard, 1964), ~~wherein the by which the~~ residual air mass becomes

393 drier with a depletion in heavy isotopes following moist adiabatic vertical ascent (Gat,
 394 1996):

$$R_r = R_0 f^{\alpha_v^l(T) - 1} \quad (812)$$

395 Here, R_r and R_0 represent the isotopic ratio of residual vapor and initial vapor,
 396 respectively. $\alpha_v^l(T)$ denotes the equilibrium fractionation factor, and f is the fraction
 397 of residual water vapor.

398 By integrating the definition of isotope ratios as given in Equation (611), the
 399 Rayleigh distillation model ~~formula~~ can be expressed in terms of isotopic content as
 400 follows:

$$\delta_r = (\delta_0 + 1) f^{\alpha_v^l(T) - 1} - 1 \quad (913)$$

401 ~~Where where~~ δ_r and δ_0 are the isotope ratios relative to ~~Vienna Standard Mean Ocean~~
 402 ~~Water (VSMOW)~~ in ~~the sample of~~ residual ~~vapor~~ and initial vapor, respectively.

403 ~~Meanwhile, wWe~~ employ the mixing model to examine the isotopic characteristics
 404 after the mixing of two air masses (Galewsky and Hurley, 2010):

$$R_{\text{mix}} = \frac{f[\text{HDO}]_1 + (1 - f) \times [\text{HDO}]_2}{f[\text{H}_2\text{O}]_1 + (1 - f) \times [\text{H}_2\text{O}]_2} \quad (1014)$$

$$R_{\text{mix}} = \frac{f[\text{H}_2^{18}\text{O}]_1 + (1 - f) \times [\text{H}_2^{18}\text{O}]_2}{f[\text{H}_2\text{O}]_1 + (1 - f) \times [\text{H}_2\text{O}]_2} \quad (15)$$

405 ~~Where where~~ R_{mix} represents the isotopic ratio of the mixed air mass, ~~while~~ $[\text{HDO}]$ ~~and~~,
 406 $[\text{H}_2\text{O}]$, ~~and~~ $[\text{H}_2^{18}\text{O}]$ denote ~~the~~ isotopic water vapor volume mixing ratios, and f is the
 407 mixing fraction.

408 ~~Given that Matara is a coastal city, we utilize a framework employing~~ ~~We use~~ water
 409 vapor isotopes to ~~study characterize the~~ mixing processes in the marine boundary layer
 410 (MBL) (Benetti et al., 2018), ~~utilizing using~~ the following equation (Craig and Gordon,
 411 1965):

$$1 + \delta_e = \frac{1}{\alpha_k} \times \frac{\alpha_{\text{eqv}}^{\text{vl}} \times (1 + \delta_{\text{OC}}) - \text{RH}_{\text{SST}} \times (1 + \delta_{\text{MBL}})}{1 - \text{RH}_{\text{SST}}} \quad (4116)$$

412 ~~Where where~~ $\alpha_{\text{eqv}}^{\text{vl}}$ represents the equilibrium fractionation factor between vapor and
 413 liquid, and α_k is the kinetic fractionation factor. δ_{OC} denotes the isotopic composition of

414 the ocean surface. We utilize $\alpha_v^{18}\text{O}$ from Majoube (1971a, b) and α_k for the smooth
415 regime ($\alpha_k^{18}\text{O} = 1.006$ and $\alpha_k\text{D} = 1.0053$) (Merlivat and Jouzel, 1979).

416 2.5 Concentration-Weighted Trajectory and Moisture Source

417 Diagnoses

418 To delineate water vapor transport paths and pinpoint moisture sources, we
419 employed the Hybrid Single-Particle Lagrange–Lagrangian Integrated Trajectory
420 (HYSPLIT) model from the US National Oceanic and Atmospheric Administration
421 (NOAA) to compute backward trajectories of air masses arriving at Matara station
422 during associated with the southwest and northeast monsoons. The Global Data
423 Assimilation System (GDAS) with $1^\circ \times 1^\circ$ and 3-hour spatial and temporal resolutions
424 furnished provided the background meteorological data from May 2020 to September

425 2020 and December 2020 to February 2021

426 (<ftp://arlftp.arlhq.noaa.gov/archives/gdas1/>). The HYSPLIT model uses GDAS
427 reanalysis data, which contains 37 (vertical) pressure levels and a $1^\circ \times 1^\circ$ horizontal
428 resolution. This enables the model to generate hourly outputs consisting of particle
429 properties, locations, and relevant meteorological variables such as pressure,
430 temperature, precipitation, and specific humidity. As atmospheric water vapor primarily
431 resides at altitudes below 2 km (Wallace and Hobbs, 2006), we initiated the backward
432 trajectories from a height of 50 m above the ground. Particles were released four times
433 daily (at 00:00, 06:00, 12:00, and 18:00 UTC) at 20 different locations within a
434 rectangular area extending 0.2° in each direction (north, south, east, and west) from
435 Matara station and at four heights above the ground (50 m, 500 m, 1200 m, and 2000
436 m). Each trajectory was back-traced for 168 h, recording data at 1-h intervals.
437 Additionally, we computed 7 day backward trajectories at 00:00h, 06:00h, 12:00h, and
438 18:00h during each monsoon period and The HYSPLIT model outputs latitude,
439 longitude, elevation, pressure, temperature, precipitation, relative humidity, and
440 specific humidity. Backward trajectory clustering analysis was conducted, using the
441 corresponding meteorological data. We averaged the trajectories of four times per day

442 to obtain a daily mean trajectory, combined with water vapor stable isotope values on
443 precipitation days. These daily mean trajectories were clustered by moisture source
444 using K-means clustering. By analyzing the variations in latitude, elevation, and
445 specific humidity along the trajectories, the influence of different moisture sources on
446 local vapor content and isotopic composition was evaluated.

447 utilized K-means clustering to calculate specific humidity along each trajectory.

448 Based on the HYSPLIT outcomes, we derived the These analyses yielded
449 concentration-weighted trajectory (CWT) fields (at a resolution of $0.5^\circ \times 0.5^\circ$) (Hsu et
450 al., 2003) using the in-situ daily average $\delta^{18}\text{O}$ and d-excess, which in turn in water vapor
451 along each backward trajectory. This facilitated the identification of potential moisture
452 sources and an assessment of the potential influence of recirculation's influence on d-
453 excess in water vapor (Salamalikis et al., 2015; Bedaso and Wu, 2020; Xu et al., 2022).
454 CWT (C_{ij}) was calculated as:

$$C_{ij} = \frac{\sum_{k=1}^K C_k \tau_{ijk}}{\sum_{k=1}^K \tau_{ijk}} \quad (4217)$$

455 Where where (i, j) denote grid coordinates, k represents the trajectory index, K is the
456 total number of trajectories analyzed, C_k is the concentration (here $\delta^{18}\text{O}$ and d-excess)
457 at the end of the trajectory k measured upon trajectory k's arrival, and τ_{ijk} is the residence
458 time of trajectory k in grid cell (i, j). During this computation, We substituted the
459 residence time is substituted by the number of trajectory endpoints in each grid cell (i,
460 j).

461

462 3 Results

463 3.1 Seasonal Variability of Water Vapor Stable Isotope

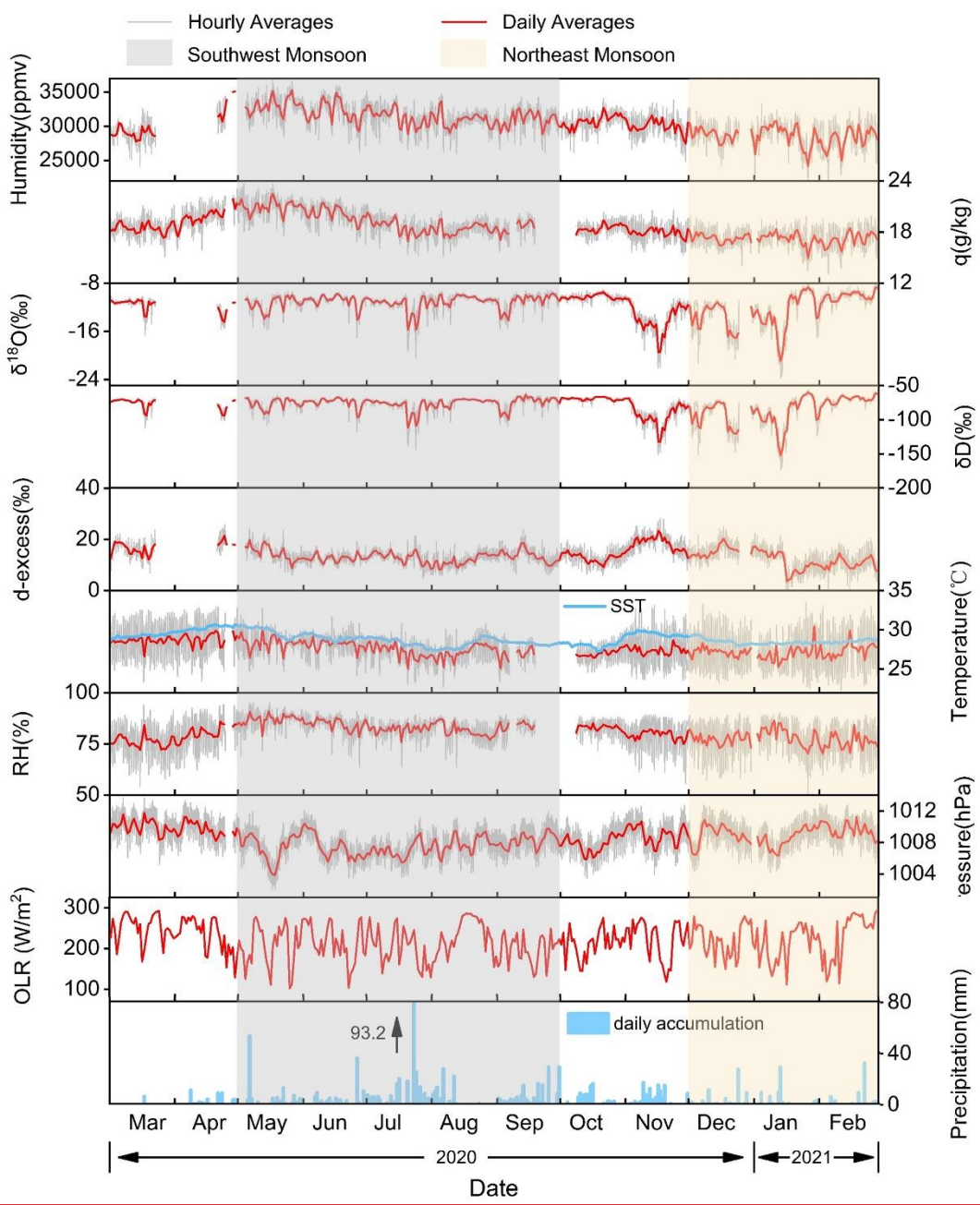
464 Figure Fig. 2 illustrates shows the hourly and daily averages of water vapor
465 isotopes ($\delta^{18}\text{O}$, δD , and d-excess) alongside temperature, relative humidity, atmospheric
466 pressure, and specific humidity from March 1, 2020, to February 28, 2021, and SST at
467 Matara station.

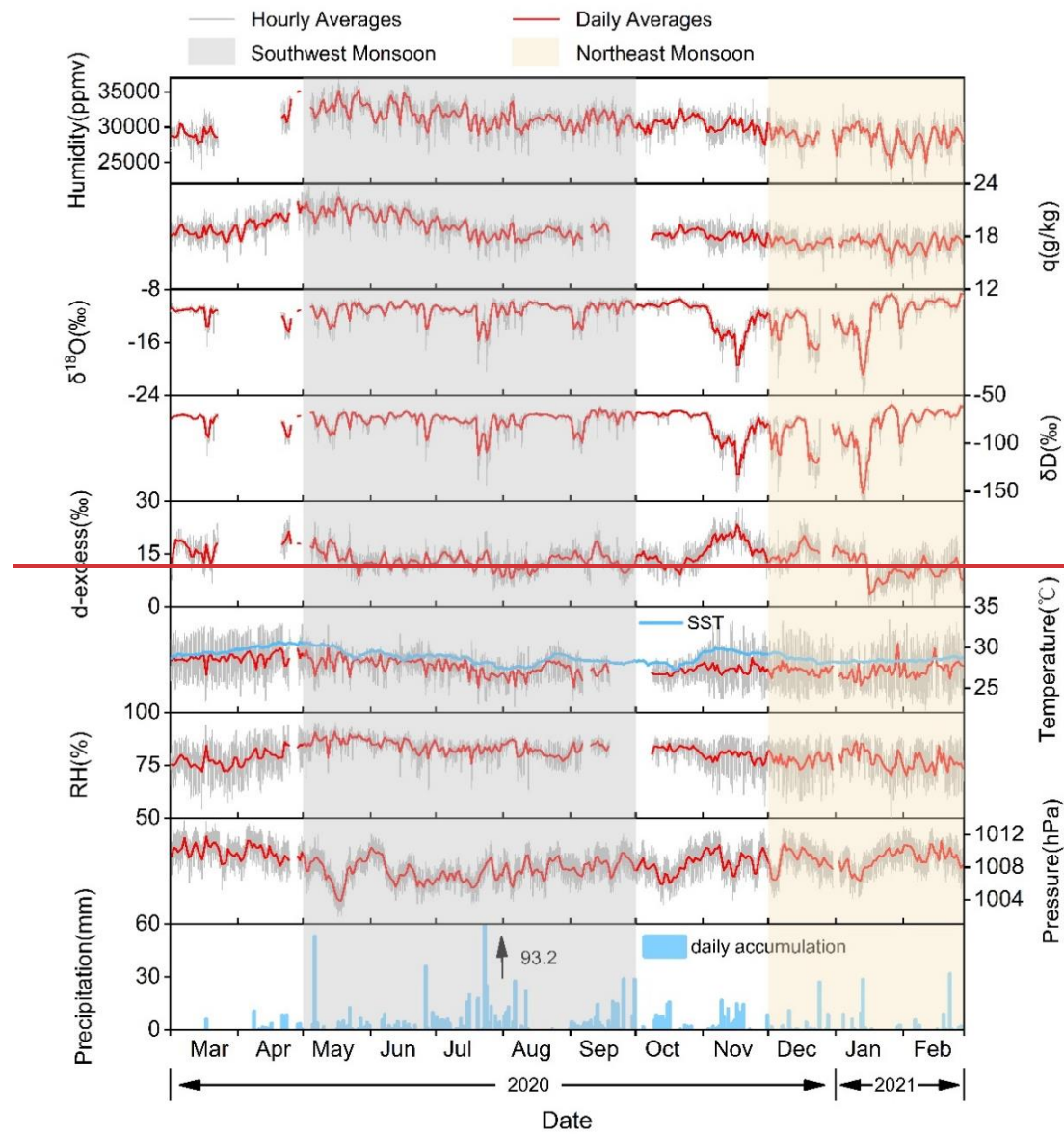
468 The mean relative humidity, specific humidity, lifting condensation level (LCL),

monthly precipitation, and water vapor isotopic composition ($\delta^{18}\text{O}$, δD , and d-excess) exhibit ~~A-a~~ clear seasonal cycle (Fig. S3 and Table 1) is evident in average values (Fig. 2 and Table 1) for relative humidity, specific humidity, lifting condensation level (LCL), monthly precipitation, and water vapor isotopic composition ($\delta^{18}\text{O}$, δD , and d-excess). Over the 12 month observation period, ~~The 12-month~~ average temperature and relative humidity ~~stand at~~ are 27.6°C and 80.7%, respectively (Table 1). Temperature variations maintain consistent amplitudes between monsoon and non-monsoon periods at around 10°C . Recorded minimum and maximum temperatures are 22.3°C and ~~24.33~~ $24.33.5^\circ\text{C}$, respectively. Specifically, comparing monthly variations in air temperature and specific humidity (Fig. S3), both parameters gradually decrease from relatively high values in May, ~~reaching to their respective minima of 26.9°C and 18.5 g/kg (monthly averages)~~ a minimum in September, ~~with monthly averages of 26.9°C and 18.5 g/kg , respectively~~. From January, ~~both~~ Monthly average air temperature and specific humidity show continuous increases, ~~from January to peaking in May with monthly averages of~~ 28.4°C and 21 g/kg in May. ~~Mean~~ Also, mean relative humidity peaks in May at 95%, with lower values observed during ~~winter the northeast monsoon~~ and ~~the~~ early first non-monsoon ~~spring~~ (December to April), reaching a minimum of 49.2% in January. From late May, specific humidity gradually declines, stabilizing after mid-July ~~and lasting~~ until October, with levels ranging from 16 g/kg to 20 g/kg . ~~During this period, significant oscillations of approximately 1.3 g/kg occur during the southwest and northeast monsoons, with corresponding amplitudes of approximately 1.3 g/kg doubled during the northeast monsoon, at approximately and~~ 2.3 g/kg , respectively. During the southwest monsoon, temperature, and specific humidity peak in May (monthly averages of $28.4 \pm 1.4^\circ\text{C}$ and $21.0 \pm 1.1 \text{ g/kg}$). February marks the coldest and driest (specific humidity) month (monthly averages of $27.4 \pm 2.6^\circ\text{C}$ and $17.1 \pm 1.3 \text{ g/kg}$) during the northeast monsoon (Fig. S3). The seasonal temperature variations exhibit modest amplitudes (Fig. 2), attributed to the tropical ~~location of the climate at~~ Matara station ~~near the equator~~. Conversely, relative humidity displays higher amplitude ~~in~~ seasonal ~~variations compared to~~ than synoptic variations. Furthermore, daily average

498 SST_s consistently exceed the daily average 2m air temperatures recorded by the AWS
499 station (Fig. 2).

500 Yearly averages for water vapor isotopic values are -11.6‰ for $\delta^{18}\text{O}$, -79.5‰ for
501 δD , and 13.3‰ for d-excess, respectively. ~~isotopic-Isotopic~~ composition ranges from
502 -23.9‰ to -7.5‰ for $\delta^{18}\text{O}$, -173.2‰ to -53.4‰ for δD , and -1.2‰ to 28.1‰ for d-
503 excess (Table 1). Monthly averages of water vapor isotopes ($\delta^{18}\text{O}$ and d-excess) exhibit
504 stability from March to October, followed by sudden decreases. $\delta^{18}\text{O}$ and δD show
505 distinct seasonal variations, with higher values during the southwest monsoon ~~period~~
506 and lower values during the northeast monsoon ~~period~~ (Table 1). Consequently, the
507 subsequent analysis will concentrate on the variations in $\delta^{18}\text{O}$. $\delta^{18}\text{O}$ decreases ~~through~~
508 ~~during the southwest monsoon, northeast non-monsoon, and non-monsoon northeast~~
509 ~~monsoon~~ periods, with mean values of -11.1‰, -14.92.2‰, and -12.21.9‰,
510 respectively. Extreme values of $\delta^{18}\text{O}$ are observed during the northeast monsoon, with
511 a maximum of -7.5‰ and a minimum of -23.9‰. Conversely, d-excess ~~follows exhibits~~
512 a reverse pattern to $\delta^{18}\text{O}$ on both seasonal and monthly scales, characterized by lower
513 values during the southwest monsoon and higher values during the non-monsoon period.
514 Furthermore, d-excess increases ~~sequentially through~~during the northeast ~~monsoon~~,
515 southwest ~~monsoon~~, and non-monsoon periods, with mean values of 12.4‰, 13‰, and
516 14.7‰, respectively. The d-excess maximum occurs in November at 28.1‰ (monthly
517 average of $15.2 \pm 4.3\text{‰}$), while the minimum of -1.2‰ ~~is-was~~ recorded in January
518 (monthly average of $11.3 \pm 4.5\text{‰}$). ~~The~~ d-excess peaks in April 2020 at 19.1‰,
519 indicating potential contributions from local recycling. The high values of d-excess are
520 related to moisture recycling. Low specific humidity corresponds to depleted $\delta^{18}\text{O}$ and
521 elevated d-excess ~~values~~, indicating a strong depletion during the long-distance
522 transport from the source regions to the observation station.





524
525 **Figure 2:** Near-surface observations at the Matara station depict of water vapor isotopes ($\delta^{18}\text{O}$,
526 δD , and d-excess) alongside local and meteorological parameters (humidity, specific humidity
527 (q), temperature, relative humidity (RH), pressure, outgoing longwave radiation (OLR,
528 obtained from NCEP), and precipitation) during non-monsoon, southwest monsoon, and
529 northeast monsoon periods from March 1, 2020, to February 28, 2021. As Matara is a coastal
530 city, local sea surface temperature at Matara (SST, obtained from ERA5) is also plotted in
531 blue.

532 **Table 1: Summary of hourly-averaged data collected at Matara station during monsoon and**
 533 **non-monsoon periods from March 1, 2020, to February 28, 2021, including averages are**
 534 **shown in (bold), standard deviations (SD), minima, maxima, and theN indicates the number**
 535 **of observations values (N) for of $\delta^{18}\text{O}$, δD , d-excess, temperature (T), relative humidity (RH),**
 536 **specific humidity (q), atmospheric boundary layer height (BLH), and lifting condensation**
 537 **level (LCL). The Yearly maximum maxima and minimum minima value for each parameter**
 538 **are highlighted using the year is all highlighted in bold italics.**

Season		$\delta^{18}\text{O}$	δD	d-excess	T	RH	q	BLH	LCL
		(‰)	(‰)	(‰)	(°C)	(%)	(g/kg)	(m)	(m)
Non- monsoon	mean	-11.9	-80.6	14.7	28.0	79.4	18.6	630.1	471.4
	SD	2.2	16.6	3.8	2.2	7.3	1.3	179.1	204.1
	Max.	-9.0	-65.3	28.1	33.2	94.2	23.0	1178.8	1283.1
	Min.	-22.1	-151.1	5.1	23.3	54.2	15.1	84.4	98.1
	N	1851	1851	1851	2617	2617	2617	2928	2617
Southwest monsoon	mean	-11.1	-75.7	13.0	27.6	83.8	19.4	741.4	348.7
	SD	1.3	9.6	2.8	1.5	4.5	1.5	149.0	118.4
	Max.	-9.1	-60.8	24.1	32.7	95.0	23.7	1564.4	938.9
	Min.	-20.4	-143.5	4.5	22.7	63.4	15.1	259.0	78.5
	N	3314	3314	3314	3192	3197	3192	3672	3192
Northeast monsoon	mean	-12.2	-85.1	12.4	27.1	77.4	17.2	516.4	524.7
	SD	3.0	22.0	4.29	2.4	7.8	1.2	139.4	224.0
	Max.	-7.5	-53.4	25.0	33.5	90.0	19.9	1125.7	1465.6
	Min.	-23.9	-173.2	-1.2	22.3	49.2	13.1	182.0	192.3
	N	1885	1885	1885	1993	1993	1993	2160	1993
All	mean	-11.6	-79.5	13.3	27.6	80.7	18.6	648.7	434.8
	SD	2.2	16.1	3.6	2.0	7.0	2.1	181.3	195.1
	Max.	-7.5	-53.4	28.1	33.5	95.0	23.7	1564.4	1465.6
	Min.	-23.9	-173.2	-1.2	22.3	49.2	13.1	84.4	78.5
	N	7050	7050	7050	7802	7807	7807	8760	7802

539

540 For $\delta^{18}\text{O}$, δD , and d-excess, synoptic variations ~~are-were also~~ recorded (Fig. 2).
541 Abrupt changes occurred in late July 2020 and from November 2020 to January 2021,
542 associated with synoptic events. Cumulative precipitation ~~for i~~ July 2020 reached 451.8
543 mm, with a notable rainfall event in late July recording daily rainfall of 93.2 mm.
544 Isotopic $\delta^{18}\text{O}$ values ~~emerged show~~ a sharp depletion from $-10.4\text{\textperthousand}$ to $-20.4\text{\textperthousand}$ within
545 20 ~~hours during of~~ isolated rainfall events., ~~lasting This depletion process of isotopes~~
546 ~~lasted~~ for 6 days. Over ~~a the~~ 75-day period spanning from late southwest monsoon to
547 mid-northeast monsoon, ~~significant noticeable~~ fluctuations ~~can be seen~~ in isotopic δ
548 ~~values range from between~~ $-22\text{\textperthousand}$ ~~to and~~ $-11\text{\textperthousand}$. ~~During~~ During the southwest monsoon
549 from July 12 to August 7, $\delta^{18}\text{O}$ values varied from $-20.4\text{\textperthousand}$ to $-9.2\text{\textperthousand}$, and δD values
550 ranged from $-143.5\text{\textperthousand}$ to $-68.6\text{\textperthousand}$. This finding is consistent with water vapor isotopic
551 $\delta^{18}\text{O}$ ($-14.1\text{\textperthousand}$ to $-9.8\text{\textperthousand}$) and δD ($-97.2\text{\textperthousand}$ to $69.1\text{\textperthousand}$) values measured from July 12 to
552 August 7, 2012, near the Bay of Bengal, although the local minimum at Matara station
553 is below the minimum in the Bay of Bengal (Midhun et al., 2013). Other coastal Stations
554 stations such as Bangalore, Ponmudi, and Wayanad, ~~all coastal like Matara, also~~
555 exhibit water vapor isotopic ~~depletion values deficient~~ in autumn and winter, mirroring
556 observations at Matara station (Table 2).

557 The atmospheric water vapor line serves as an indicator of the humidity conditions
558 at the vapor source and the fractionation processes along the transport path. The slope
559 reflects the extent of vapor kinetic fractionation ~~the vapor has experienced~~, while the
560 intercept indicates the humidity levels at the vapor source. Comparing the Local
561 Meteoric Water Line (LMWL) for $\delta^{18}\text{O}$ and δD , ~~compared~~ with the Global Meteoric
562 Water Line (GMWL), ~~shows we obtain~~ a slope of < 8 during both monsoon periods
563 (Fig. 3a). Seasonal variations are also visible in $\delta^{18}\text{O}$ and δD distribution patterns. Daily
564 averages of water vapor isotopic $\delta^{18}\text{O}$ and δD demonstrate a strong correlation ($r = 0.96$)
565 ~~with a slope of = 7.26~~ with a lower intercept ~~of at~~ 4.68. During the northeast
566 monsoon, LMWL slope and intercept are higher compared to other periods, indicating
567 significant moisture recirculation. During ~~The the~~ southwest monsoon, ~~lower both the~~
568 slope (6.93) and intercept (1.18) are ~~lower exhibited~~ compared to other periods,

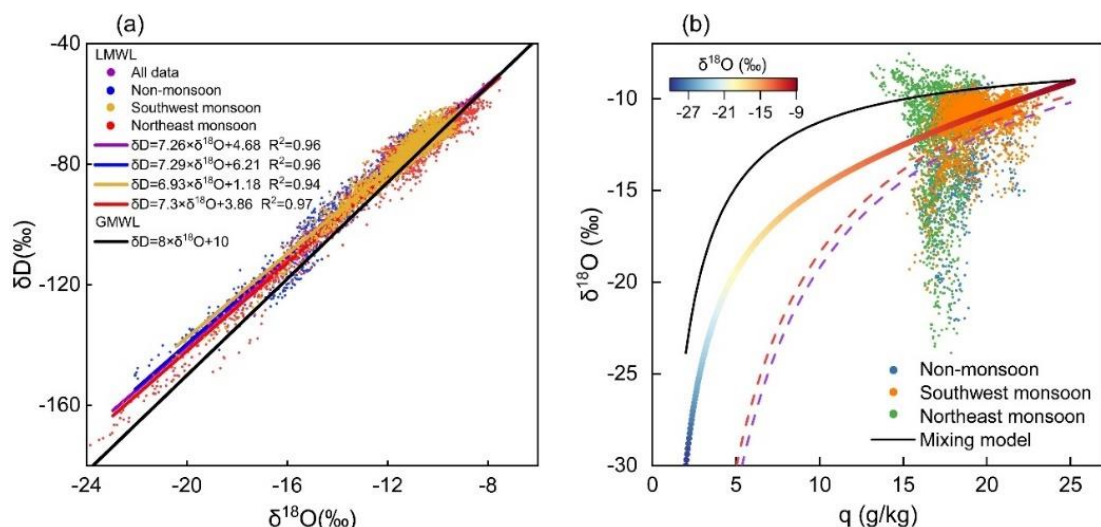
569 correlating with higher rainfall (Fig. 2).

570 **Table 2: Summary of observed water vapor isotope concentrations at various stations in India**
 571 **and the Bay of Bengal, showing variations within each period.**

Country or region	Station or location	Latitude (N°)	Longitude (E°)	Date	$\delta^{18}\text{O}$ (‰)	δD (‰)	d-excess (‰)	References
India	Bangalore	13.01	77.55	Jun 1, 2012, to	-23.8	-178.3	-4.5 to	
				Sep 30, 2012	to -9.0	to -58.6	32.7	
				Oct 1, 2012, to	-22.7	-177.1	-9.5 to	(Rahul et al., 2016b)
				Feb 28, 2013	to -10.2	to -73.7	41.4	
	Kolkata	22.56	88.41	May 3, 2019, to	-16.9	-128.3	-7.1 to	
				Oct 25, 2019	to -10.0	to -72.8	25.4	(Bhattacharya et al., 2021)
	Roorkee	29.87	77.88	Feb 1, 2007, to	-17.0		32.0 to	
				May 31, 2007	to -3.0		70.0	
				Jun 1, 2007, to	-32.0	none	40.0 to	
				Sep 30, 2007	to -6.0		87.0	(Saranya et al., 2018)
Bay of Bengal	Ponmudi	8.76	77.12	Oct 1, 2007, to	-30.0		30.0 to	
				Dec 31, 2007	to -7.0		60.0	
	Wayanad	11.51	76.02	Apr 1, 2012, to	-24.1	-170.0	6.3 to	
				Nov 30, 2012	to -8.6	to -51.0	26.5	(Lekshmy et al., 2018)
	Ahmedabad	23.03	72.56	Apr 1, 2007, to	-20.5	-139.1	13.3 to	
				Apr 1, 2008	to -7.9	to -50.0	31.2	
	Chhota Shigri	32.58	77.58	Apr 1, 2007, to	-19.2	-128.1	6.9 to	
				Apr 1, 2008	to -8.9	to -59.8	40.4	(Srivastava et al., 2015)
	6m	32.58	77.58	Apr 1, 2007, to	-19.4	-101.5	28.0 to	
				Apr 1, 2008	to -10.3	to -29.2	62.0	(Ranjan et al., 2021)
Bay of Bengal	25m	25m	none	Jul 1, 2012, to	-13.6	-94.0 to	5.7 to	
				Aug 1, 2012	to -10.0	-68.3	16.4	(Midhun et al., 2013)
	25m	25m	none	Nov 15, 2013, to	-14.1	-97.2 to	6.9 to	
				Dec 1, 2013	to -9.8	-69.1	19.4	

572 ~~The observation period revealed~~ We found a significant negative relationship
 573 between $\delta^{18}\text{O}$ and d-excess, ~~where the~~ with a rate of change for d-excess with $\delta^{18}\text{O}$ is -
 574 0.68 ‰/‰ (r = -0.55) (Fig. S4a), ~~which~~. This is below the -1.40.05 ‰/‰ recorded at
 575 the ~~the~~ ~~Bangalore~~ southern Greenland Ivittuut station ~~and the~~ 1.2 - 1.1 ‰/‰ range
 576 observed at NEEM station during the summer (Rahul et al., 2016b; Steen Larsen et al.,

577 2013b; Bonne et al. 2014). Seasonally, the correlation between ~~the two~~both variables
 578 weakens ~~sequentially~~ during the southwest monsoon period, northeast monsoon period,
 579 and ~~the~~ non-monsoon periods. ~~The, with respective~~ rates of change ~~are of~~ -0.94 ‰/‰
 580 ($r = -0.49$), -0.69 ‰/‰ ($r = -0.54$), and -0.65 ‰/‰ ($r = -0.44$), ~~respectively~~. Similar
 581 patterns are detected for temperature-d-excess and specific humidity-d-excess
 582 correlations. ~~This pattern aligns with the incremental rise showing gradual increases~~ in
 583 the ~~slopes~~ and ~~intercepts~~ of the water vapor line. Moreover, the concentrated
 584 distribution of vapor values during the southwest monsoon and the highly scattered
 585 distribution during the northeast monsoon are indicative of the corresponding seasonal
 586 distributions of the water vapor line.



587 **Figure 3: (a)** Co-variation of water vapor isotopic composition and meteorological parameters
 588 during different monsoon and non-monsoon periods ~~from between~~ March 1, 2020, ~~to and~~
 589 February 28, 2021. The lines represent linear least-squares regressions (LMWL and GMWL)
 590 of δD (‰) as a function of $\delta^{18}\text{O}$ (‰). **(b)** Scatter plot of observed hourly water vapor isotopic
 591 $\delta^{18}\text{O}$ vs. specific humidity (q). The ~~dotted-dashed~~ red and blue ~~curves~~ represents the Rayleigh
 592 distillation line during the southwest monsoon. ~~The dotted blue curve represents the Rayleigh~~
 593 ~~distillation line during the~~ northeast monsoon. The solid black curve represents the mixing
 594 line. The ~~colorful-colored~~ curve represents the MBL-mixing line.
 595

596 ~~The Plots of q - $\delta^{18}\text{O}$ plots, the combined with theoretical Rayleigh distillation~~
 597 ~~curve, the mixing curve line, and MBL-mixing curve, were utilized used~~ to assess
 598 mixing conditions during the ~~studied study~~ periods (Fig. 3b). During the southwest

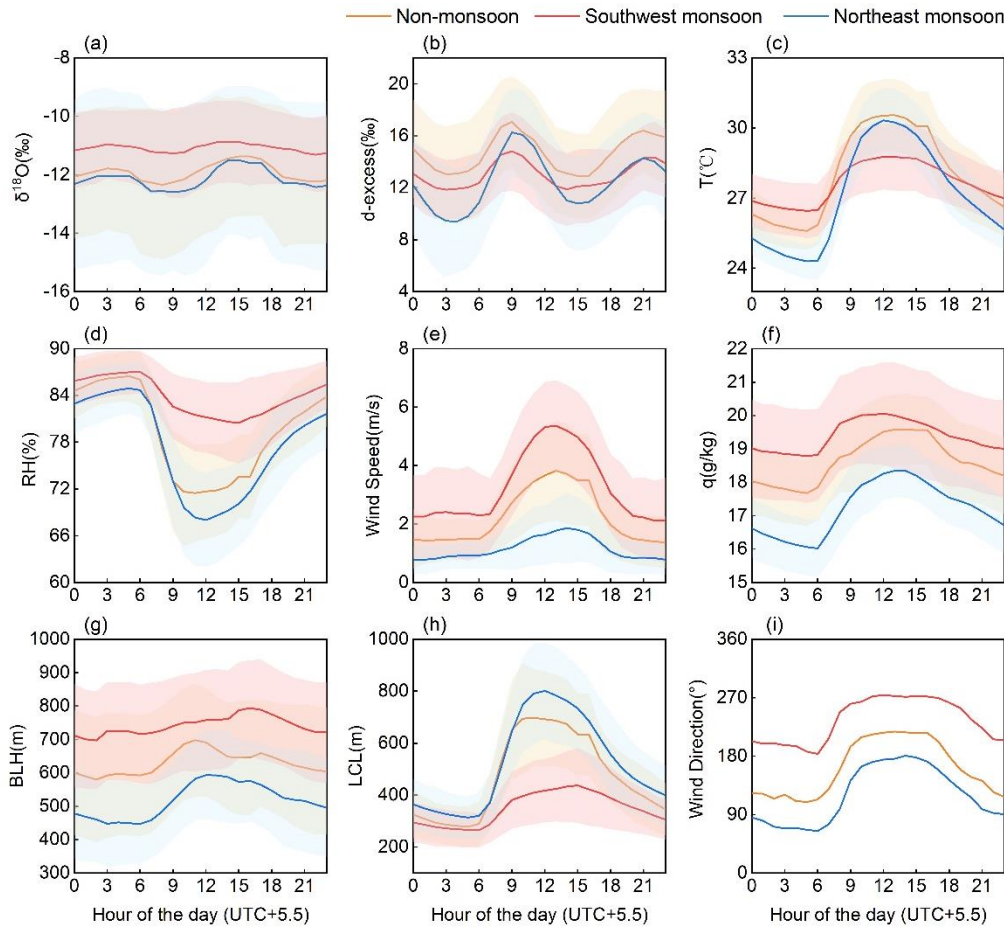
599 monsoon, most measurements are clustered between the Rayleigh ~~curve~~ and mixing
600 curve, indicating isotopic variability dominated by leaching effects of precipitation
601 ~~leaching process~~ and moisture mixing process. Limited water vapor measurements are
602 scattered below the Rayleigh fractionation line, implying a discernible impact of
603 raindrop re-evaporation. Similarly, during the non-monsoon period, most
604 measurements ~~are lie observed~~ between the Rayleigh ~~curve~~ and mixing curves, with
605 only a few located below the Rayleigh line. During the northeast monsoon, $\delta^{18}\text{O}$ spans
606 ~~both from the~~ upper ~~and to the~~ lower ~~sides extreme~~ of the mixing ~~curve~~ and Rayleigh
607 distillation curves. The measurements substantially deviated ~~from~~ from the Rayleigh curve
608 and ~~more show a higher depleted depletion than predicted by the~~ Rayleigh
609 ~~prediction model, which is~~ likely due to the influence of convective processes.

610 3.2 Diurnal Cycles

611 To ~~evaluate look for~~ diurnal cycles in isotopic composition and meteorological
612 parameters, we analyzed hourly averages ~~at Matara station, particularly focusing on the~~
613 ~~pronounced diurnal patterns during the northeast monsoon characterized by stable~~
614 ~~weather conditions (low horizontal wind speed)~~ (Fig. 4c-e).

615 All ~~water vapor~~ isotopic ~~signals~~ ($\delta^{18}\text{O}$, δD , and d-excess) and meteorological
616 parameters exhibit strong diurnal variations during both monsoon and non-monsoon
617 periods (Fig. 4). Overall, the diurnal variations ~~of in~~ local meteorological ~~factors~~
618 ~~reflects the dynamic changes in the atmospheric boundary layer at Matara. During the~~
619 ~~daytime, as parameters~~ solar radiation ~~during the day and the resulting development of~~
620 ~~a intensifies and the~~ boundary layer ~~develops, with increasing~~ temperatures and wind
621 speeds ~~increase from between~~ noon ~~to and the~~ afternoon, accompanied by a decrease in
622 relative humidity ~~and led due~~ to significant evapotranspiration. At night, surface
623 radiative cooling causes temperatures to drop, resulting in ~~calmer conditions near the~~
624 ~~surface calm conditions~~ and gradual air saturation, ~~which points to indicating~~ a
625 relatively stable atmospheric boundary layer. During the southwest monsoon, $\delta^{18}\text{O}$, δD ,
626 relative humidity, wind speed, specific humidity, and BLH are generally higher than
627 ~~during~~ the northeast monsoon and non-monsoon periods, while d-excess and LCL are

lower. In the early morning, $\delta^{18}\text{O}$ values steadily ~~dropdecreases~~, reaching ~~their lowest levels a minimum~~ (-11.26‰) ~~at~~ around sunrise (~09:00 local time (LT)). Subsequently, ~~they it~~ increases throughout the day, peaking (-10.87‰) in the afternoon (~15:00 LT), ~~with yielding~~ a diurnal fluctuation of merely 0.45‰. Increased specific humidity between 10:00 LT and 14:00 LT coincides with ~~rises in increasing~~ air temperatures and wind speeds and ~~a decline in decreasing~~ relative humidity (Fig. 4c-f). BLH peaks between 14:00 LT and 16:00 LT, slightly ~~delayed compared to later than~~ other meteorological parameters. ~~Conversely T, the northeast monsoon exhibits reversed he same~~ diurnal variations for each parameter ~~were observed during the northeast monsoon. During the northeast monsoon, the daily variations of $\delta^{18}\text{O}$ and d-excess are significant, with the maximum amplitude changes in $\delta^{18}\text{O}$ and d-excess of at 1.1‰ and 6.8‰, respectively. Specific humidity peaks from between 10:00 LT to and 16:00 LT, accompanied by increases in air temperature, wind speed, BLH, and LCL. After 16:00 LT, specific humidity decreases alongside declines in isotopic δ values and other meteorological parameters. The d-excess peaks (14.81‰) at 09:00 LT and fluctuates until 23:00 LT, contrasting with the period from 04:00 LT to 09:00 LT (Fig. 4b). The d-excess exhibits a W-shaped variability, reaching similar highs at 09:00 LT and 21:00 LT. Specific humidity exhibits a diurnal variation that aligns closely with the $\delta^{18}\text{O}$ pattern, reaching its minimum before sunrise and peaking around midday (10:00-15:00 LT). From the Between afternoon to and evening, specific humidity stays remains relatively high and stable. The diurnal variation during the southwest monsoon and northeast monsoon periods is are 1.28 g/kg and 2.32 g/kg, respectively. Similarities with patterns observed at Lena station patterns (Bonne et al. 2020) suggest potential influences from moisture exchange between the atmosphere and the ocean surface, particularly during the northeast monsoon.~~



653

654 **Figure 4: Depicts a Average diurnal cycles of (a) $\delta^{18}\text{O}$, (b) d-excess, (c) temperature (T), (d)**
 655 **relative humidity (RH), (e) wind speed, (f) specific humidity (q), (g) atmospheric boundary**
 656 **layer height (BLH), (h) lifting condensation level (LCL), and (i) wind direction during the non-**
 657 **monsoon, southwest monsoon, and northeast monsoon periods. Shaded areas correspond to**
 658 **±1 standard deviation.**

659 **3.3 Sea Surface Evaporation Conditions in the Moisture Source**
 660 **Region**

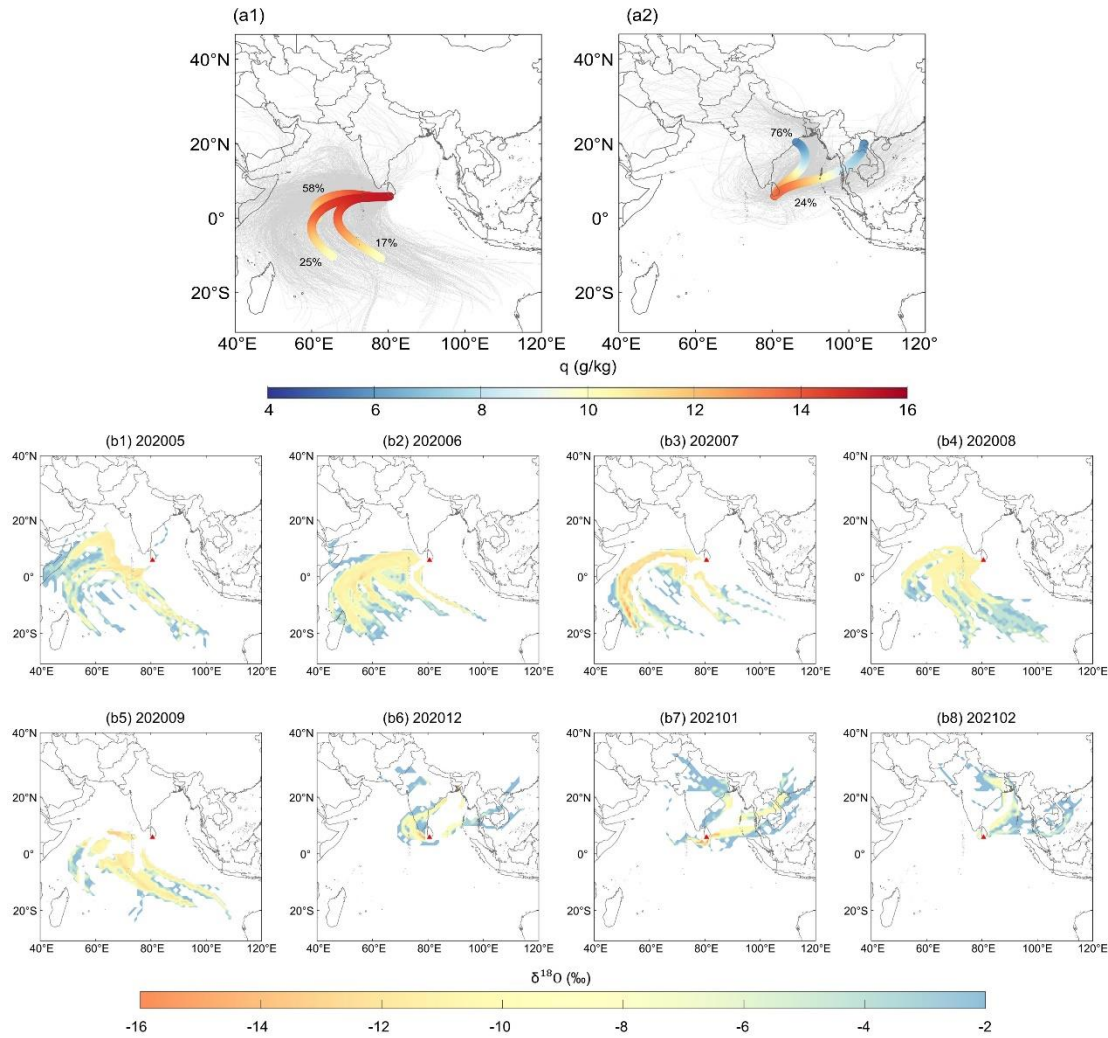
661 To be able to explore water vapor isotopic variations in the sea surface boundary
 662 layer, we must first Understanding understand the processes and factors that affect
 663 influencing water stable isotopic isotope variations in during ocean surface water
 664 evaporation is crucial for exploring water vapor isotopic variations in the sea surface
 665 boundary layer. The primary determinant governing water vapor stable isotope shifts
 666 across different regions is the regional moisture transport process, characterized by

667 differences in isotopic variations in the moisture source region, variations in
668 meteorological conditions during the evaporation processes, and divergences of the
669 moisture transport pathways (Bonne et al., 2020). Thus, this section aims to ~~reveal~~
670 ~~essential~~identify factors ~~that~~drivingdrive the seasonal variationss of near-surface
671 atmospheric water vapor stable isotopes at Matara, including water vapor origins,
672 transmission routes, and sea surface evaporation conditions in the source regions.

673 To further understand the different seasonal relationships between $\delta^{18}\text{O}$, d-excess,
674 and meteorological parameters, we analyzed potential seasonal differences ~~in~~between
675 the main moisture sources ~~for water vapor transported to Matara Station during the~~
676 ~~2020-2021 southwest monsoon and northeast monsoon by using~~ HYSPLIT. Trajectories
677 ~~that reach Matara~~ during the southwest ~~monsoon~~ and northeast monsoons ~~show~~have
678 different origins ~~of water vapor~~. During the southwest monsoon, wind directions span
679 from 60° to 360° and the main origin regions are mostly in~~therefore~~ the Arabian Sea
680 (AS) and Indian Ocean (Fig. 5a). ~~due~~Due to the northward movement of the warm
681 South Equatorial Current, these winds gather significant amounts of moisture along the
682 way, bringing heavy rainfall to Matara (Fig. 5a). Conversely, during the northeast
683 monsoon, the main wind direction shifts to 0°-225° and 330°-360°, such that most
684 trajectories originate in northeast India, where with lower specific humidity is lower
685 ~~(due to overland)~~airflow, and only a short portion of the trajectory passes over ~~small~~
686 ~~part from~~ the BoB. The long transport distance results in a greater~~more~~ depletion ~~of~~in
687 water vapor isotopes once the air mass arrives at Matara station.

688 ~~We calculated water vapor sources at Matara station for each month during the two~~
689 ~~monsoon seasons. Fig. 5a shows that the primary moisture sources are the Indian Ocean~~
690 ~~to the southwest and the BoB to the northeast of Matara. During the southwest monsoon,~~
691 ~~water vapor predominantly originates from the Indian Ocean, encompassing wind~~
692 ~~directions spanning 60° to 360°. Conversely, during the northeast monsoon, the primary~~
693 ~~water vapor source shifts to the BoB, featuring wind directions from 0° to 225° and 330°~~
694 ~~to 360° to exclude the influence of inland water vapor.~~ Moisture from all sources shows
695 seasonal variations, with depleted $\delta^{18}\text{O}$ values lower during the southwest monsoon

696 ~~than and enriched $\delta^{18}\text{O}$ values~~ during the northeast monsoon. The shift in water vapor
 697 source from the AS ~~in May~~ to the southern Indian Ocean ~~in between May and~~
 698 September leads to ~~enriched water vapor~~ $\delta^{18}\text{O}$ ~~enriched water vapor values~~ from August
 699 to September. Enhanced convective activity and rainfall during the southwest monsoon
 700 result in $\delta^{18}\text{O}$ depletion, while tropical storms and hurricanes also contribute to $\delta^{18}\text{O}$
 701 depletion.



702
 703 **Figure 5: Backward trajectories of water vapor tracks reaching Matara station ~~and its four~~**
 704 **~~surrounding sites (height-of-50m, 500m, 1200m, and 2000m)~~ during the (a1) southwest**
 705 **~~monsoon and (a2) northeast monsoon. The changes in specific humidity (q) along each~~**
 706 **~~clustered trajectory are shown in color. The black numbers indicate the percentages,~~**
 707 **~~reflecting the proportion (%) of trajectories represented by each clustered trajectory.~~**
 708 **Monthly concentration fields of water vapor isotopic $\delta^{18}\text{O}$ for from a 168h HYSPLIT**

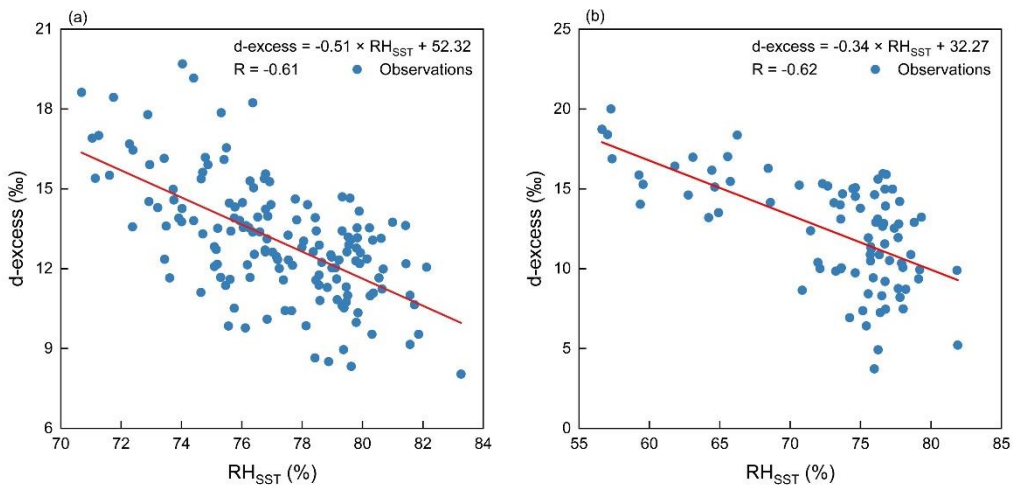
709 simulation of back trajectories during the two monsoon seasons (b1-b8). Red triangle marks
710 the study site.

711 Similar seasonal variations are observed in d-excess exhibits similar seasonal
712 variations values at Matara station, with lower values during the two monsoon seasons
713 and higher values in during the non-monsoon periods (refer to Table 2, Fig. 4). This
714 seasonal variation in d-excess may stem from changes in relative humidity in the
715 moisture source areas and further modifications during moisture transport.

716 Ocean evaporation represents the starting point of the phase transformations that
717 occur within the global water cycle. Identifying the isotopic variations and controlling
718 factors of oceanic evaporation is essential for understanding isotopic shifts in the
719 marine boundary layer. Previous coastal observational studies in focusing on the marine
720 boundary layer have confirmed a significant association between d-excess monitored
721 at coastal observation stations and RH_{SST} in the proximate oceanic source areas (Pfahl
722 and Wernli, 2009; Steen-Larsen et al., 2015). In cases where dynamic fractionation
723 during air mass transport is either absent or minimal, d-excess can serve as an indicator
724 of the moisture source region (Bonne et al., 2014).

725 The map of the moisture sources (Fig. 5) identified the Indian Ocean and BoB as
726 the main source areas for moisture arriving at Marara station. To gauge the impact of
727 more local influences, we investigated how changes in sea surface meteorological
728 conditions in the sea around Matara station affects near surface water vapor isotope
729 concentrations (Fig. S6). During the southwest monsoon, RH_{SST} values in "region
730 Region a" (located to the south of Matara between 3-6°N and 78-82°E) ranged from
731 66% to 84%, with SST fluctuating between 28.0°C and 30.6°C. During the northeast
732 monsoon, RH_{SST} values in "region Region b" (located to the east of Matara between 6-
733 8°N and 82-85°E) ranged from 54% to 84%, with SST fluctuating between 28.1°C and
734 29.1°C. In comparison with the southwest monsoon, RH_{SST} is slightly lower exhibits a
735 comparatively drier tendency, accompanied by less pronounced variability in SST. The
736 rate of change in d-excess under the influence of RH_{SST} in the BoB (during the northeast
737 monsoon) is -0.34 ‰. In comparison, the rate of change in d-excess with the RH_{SST}

738 of the northern Indian Ocean (during the southwest monsoon) is -0.51 ‰ , suggesting
 739 that the evaporation from over the northern Indian Ocean significantly impacts local d-
 740 excess. Studies focused on the BoB's sea surface of BoB revealed that RH_{SST} explains
 741 only 25% of the d-excess variation (d-excess = $(-0.55 \pm 0.14) \times \text{RH}_{\text{SST}} + (56 \pm 12)$; $r =$
 742 -0.5). The limited variation in relative humidity during the monsoon period led to a
 743 low diminish the correlation, indicating that monsoon moisture plays a crucial role in
 744 the isotopic composition of water vapor in the BoB (Midhun et al., 2013). Conversely,
 745 the observed relationship between near-surface water vapor d-excess at Matara and
 746 relative humidity in the surrounding oceanic region during the observational period,
 747 with correlation coefficients of -0.61 and -0.62 ($p < 0.01$), respectively (Fig. 6), reveals
 748 a marked negative correlation between d-excess and relative humidity in the nearby
 749 Indian Ocean and BoB, indicating that water vapor at Matara is predominantly supplied
 750 by nearby oceans the adjacent marine environment. Notably, SST amplitude near the
 751 Matara station is smaller than the variations in near-surface air temperature (as
 752 depicted by the SST line in Fig. 2).



753
 754 **Figure 6:** illustrates the relationship between d-excess and RH_{SST} during the (a) southwest
 755 monsoon and (b) northeast monsoon. Specific sea regions (Fig. S6) to the south (Region a: 3-
 756 6°N and 78-82°E) and east (Region b: 6-8°N and 82-85°E) of the observation station were
 757 selected to investigate the impact of sea surface meteorological conditions on near-surface
 758 water vapor isotopes during the two monsoon periods.

759 **3.4 Influence of Convective Activity**

760 In the equatorial tropics, OLR mainly results from convective activity and cloud
761 cover, which can impact the stable ~~isotopic-isotope~~ composition of precipitation
762 (Ohring et al., 1984; Gao et al., 2013; Guo et al., 2017). Generally, higher OLR values
763 are associated with weaker convective activity. Examining the correlation between
764 stable isotopes of water vapor and OLR helps to understand the impact of convective
765 activities along near-surface trajectories of water vapor stable isotopes at Matara station.

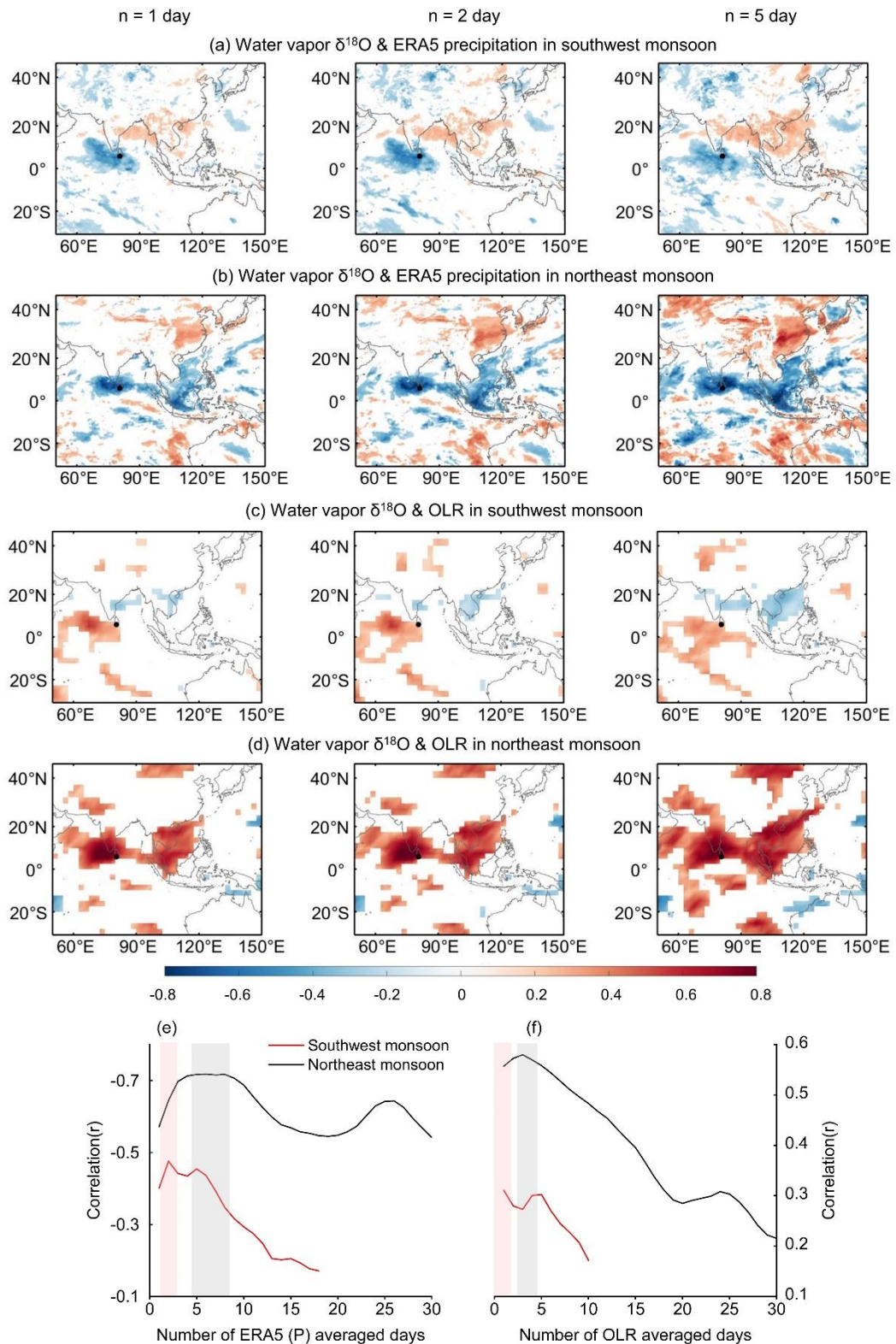
766 We calculated ~~the spatiotemporal correlation of between OLR, and precipitation~~
767 amount ~~with using~~ the measured water vapor isotopic compositions at Matara station,
768 ~~covering the period from March 2020 to February 2021. For each grid point in this~~
769 ~~region~~Specifically, we calculated ~~the average precipitation amount for each grid point~~
770 by averaging over different numbers of days (n = 1, 2, up to 30) preceding each
771 precipitation day. Lower OLR values ~~represent indicate~~ the presence of deep convective
772 clouds in this region, ~~indicating relatively and~~ higher precipitation ~~and~~ associated with
773 lower δ values.

774 ~~Figure Fig. 7a represents shows~~ the strong positive correlation (red regions)
775 between rainfall and $\delta^{18}\text{O}$ during the southwest monsoon, mainly in the ~~northern~~ BoB
776 and ~~over~~ India. This correlation strengthens and extends over wider areas as n increases
777 from 1 to 5. Additionally, a strong negative correlation is evident in the northern Indian
778 Ocean and southern Arabian Sea, ~~with correlations~~ reaching a maximum for n = 2 ~~days~~.
779 During the northeast monsoon, the spatial correlation distribution differs, with a
780 negative correlation observed ~~in over~~ the southern Indian Ocean and BoB (Fig. 7b).
781 Lower OLR values in the Arabian Sea, the southern part of the BoB, and throughout
782 Southeast Asia correspond to a decrease in water vapor isotopic $\delta^{18}\text{O}$ at Matara station
783 (Fig. 7c, d). This pattern indicates that water vapor $\delta^{18}\text{O}$ during the northeast monsoon
784 period is influenced by convective activities ~~in over~~ the Arabian Sea, South BoB, and
785 Southeast Asian regions. The stronger ~~the this~~ convective activity, the more depleted ~~is~~
786 ~~the air reaching Matara in~~ water vapor isotopic $\delta^{18}\text{O}$ ~~the air reaching Matara becomes~~.

787 To examine the correlation between water vapor isotopic $\delta^{18}\text{O}$ and local

788 precipitation (Fig. 7e) and OLR (Fig. 7f), we ~~choose-selected~~ a small region of $5^\circ \times 5^\circ$
789 ~~with-around~~ Matara and calculated the time- and space- correlation for all grid points
790 as described above. The results show that the correlation with precipitation is negative
791 during both monsoon seasons as expected. The depletion of low-level water vapor $\delta^{18}\text{O}$
792 is related to the transport and deposition of water vapor into the lower atmosphere
793 through convective activity (Kurita, 2013; Midhun et al., 2013; Lekshmy et al., 2014).
794 The air masses are re-supplied to the convective system through moisture recycling.
795 This results in a strong correlation between the isotopic composition of water vapor and
796 the convective activity ~~of~~ ~~during~~ the previous day (Fig. 7e and 7f). ~~The~~ ~~R~~esidual water
797 vapor is more depleted in strong convective systems. In our study, the correlation
798 reaches a high value after about 5 days, indicating that the convective activity is
799 sufficiently established to affect the isotopic composition of water vapor. In fact, the
800 correlation (for $p < 0.05$ and in absolute terms) is ~~indeed~~ high for all n values, with
801 maxima of about 0.48 for $n = 3$ ~~days~~ during the southwest monsoon and ~~about~~ 0.72 for
802 $n = 4$ to 9 ~~days~~.

803 The OLR correlation peaks at smaller time scales (~~refer to Fig. 7f~~, (approximately
804 $n = 1-4$ days, Fig. 7f), ~~in contrast to~~ ~~than~~ precipitation, ~~which peaks over larger time~~
805 ~~scales of ($n = 3-8$ days)~~. We attribute this difference to the effect of cloud distribution
806 on precipitation and OLR. OLR has a stronger response to shallow clouds, while
807 precipitation is more responsive to both deep convective clouds and shallow clouds
808 (Masunaga and Kummerow, 2006; Schumacher, 2006). The OLR minimum occurs
809 when thunderstorm clouds result in more precipitation. Additionally, deep thunderstorm
810 clouds, with short lifetimes and consequently very low OLR (corresponding to highly
811 depleted water vapor isotopic δ), exhibit a short memory effect on the correlation (peak
812 occurs at smaller time scales) (Gambheer and Bhat, 2000).



813

814 **Figure 7: Spatial correlation fields of water vapor isotopic composition and averaged ERA5**
 815 **precipitation (P) during the (a) southwest monsoon and (b) northeast monsoon, along with the**
 816 **spatial correlation fields ~~of~~ for average outgoing longwave radiation (OLR) during the (c)**
 817 **southwest monsoon and (d) northeast monsoon. Averaging was conducted at each grid point**

818 for three periods of $n = 1, 2$, and 5 days preceding each of the 153 days of the southwest
819 monsoon (a, c) and 90 days of the northeast monsoon (b, d). Correlation between (e) $\delta^{18}\text{O}$ and
820 (e) P, as well as along with (f) $\delta^{18}\text{O}$ and OLR during the southwest monsoon (red line) and
821 northeast monsoon (black line) for values over n days ($n = 1, 2, 3, \dots 30$). Red (grey) areas
822 shows the n -range with for which the highest correlation was obtained during southwest
823 monsoon (northeast) monsoon. Here, n represents the average "moisture mixing time" of
824 regional precipitation, affecting water vapor isotopes through the transport of residual water
825 vapor (Rahul et al., 2016b).

826 During both the southwest and northeast monsoons, $\delta^{18}\text{O}$ exhibits a weak
827 correlation with 2m air temperature (Fig. S7) for the simultaneous values. Throughout
828 the year, the relationship between 2m air temperature and $\delta^{18}\text{O}$ in water vapor is $\delta^{18}\text{O}$
829 = $0.7T - 30.8$ ($r = 0.32$) (Fig. S9). During the southwest and northeast monsoons, the
830 relationships become $\delta^{18}\text{O} = 0.5T - 24.95$ ($r = 0.39$) and $\delta^{18}\text{O} = 1.46*T - 51.71$ ($r =$
831 0.43), respectively (Fig. S7). Daily temperature and $\delta^{18}\text{O}$ values fluctuate less during
832 the southwest monsoon than in during the northeast monsoon period (Fig. 4), possibly
833 due to a weaker temperature inversion during the southwest monsoon.

834 The correlation between $\delta^{18}\text{O}$ and relative humidity differs between the two
835 monsoon periods. During the southwest monsoon, $\delta^{18}\text{O}$ and relative humidity appear
836 uncorrelated ($r = 0.01$), consistent with previous findings (Rahul et al., 2016b).
837 Conversely, during the northeast monsoon, a robust negative correlation emerges
838 between $\delta^{18}\text{O}$ and relative humidity ($r = -0.58$). Similarly, the relationship between $\delta^{18}\text{O}$
839 and precipitation varies between both monsoon seasons (Fig. S7). Moreover, during
840 the southwest monsoon, heavy precipitation leads to relatively high relative humidity
841 and the enrichment of heavier isotopes.

842

843 **4. Discussion**

844 This study presented the results from a one-year (March 2020 to February 2021)
845 in-situ measurement campaign of near-surface atmospheric water vapor isotopes ($\delta^{18}\text{O}$,
846 δD) at Matara station, Sri Lanka. These high-temporal resolution water vapor isotopic

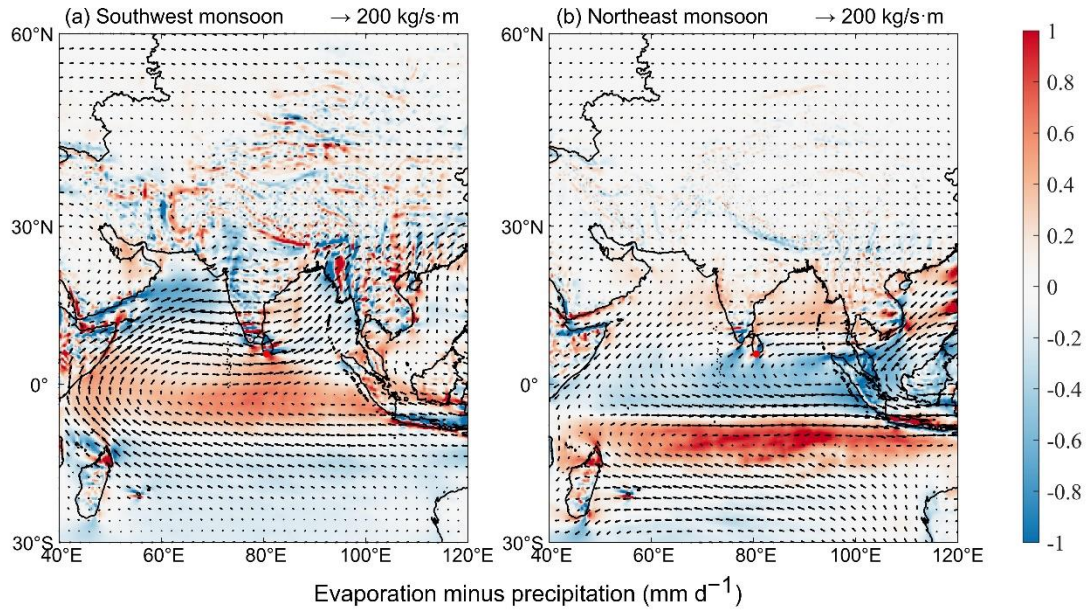
847 composition and meteorological observations provided a good opportunity to
848 investigate the water vapor isotopic dynamics from synoptic to seasonal scales. The
849 variability of water vapor isotopes at Matara station is influenced by local
850 meteorological factors, oceanic evaporation processes, and regional convective
851 activities, depending on the water sources and moisture transport. The measurements
852 provided insights into multi-time-scale variations in near-surface atmospheric water
853 vapor in an equatorial region and provided information about the interactions between
854 large-scale atmospheric moisture transport and oceanic evaporation.

855 **4.1 Seasonal Versus Synoptic Variabilities and Water Vapor Flux**

856 To evaluate the influence of seasonal variations in moisture sources on the stable
857 water vapor isotopic composition, we focus on how changes in specific humidity and
858 isotopes relate to observed variations in wind direction at Matara station (Fig. S11).
859 During the southwest monsoon, the distribution of wind directions appears relatively
860 narrow, and the highest specific humidity values were recorded for west-north-westly
861 (WNW) wind directions (Fig. S11). $\delta^{18}\text{O}$ values were highest and d-excess lowest if the
862 moisture source area was to the west of Matara, while $\delta^{18}\text{O}$ depletion and high d-excess
863 were associated with air masses that arrived from the east (Fig. S11). The southwest
864 monsoon period exhibits similar ranges of specific humidity and water vapor isotope
865 composition irrespective of wind direction. During the northeast monsoon, the
866 northeastern winds from BoB brings a higher proportion of more dry air, resulting in
867 the range of specific humidity between 14 and 17 g/kg (Fig. S11) and isotopically
868 depleted water vapor ($\delta^{18}\text{O} < -22\text{\textperthousand}$) compared to other regions. Thus, these air masses
869 undergo considerable isotopic fractionation as they pass overland before reaching our
870 measurement site. For air masses originating in the southeast and northwest, isotopic
871 composition may be influenced by closer moisture sources, associated with the
872 considerable moisture uptake observed over the Arabian Sea and northern Indian Ocean
873 (Fig. S12). With easterly and northeasterly winds $\delta^{18}\text{O}$ is often elevated, with $\delta^{18}\text{O}$
874 (exceeding $-10\text{\textperthousand}$) associated with the northwesterlies (Fig. S11).

875 Since the local wind direction only provides information on the final stage of air

mass transport, we conduct a more detailed analysis of how water vapor flux, evaporation, and precipitation along the transport pathway affect local variations in stable water vapor isotopes. During the southwest monsoon, evaporation rates at Matara station are lower than precipitation rates (Fig. S12), something we also observed over the central Indian Ocean. In contrast, over the northern Indian Ocean and western BoB, located up and downstream from Matara station, we obtained a water vapor budget where evaporation exceeded precipitation. During the northeast monsoon, the Matara region is affected by moisture sources from the BoB and South Asia, resulting in higher evaporation rates than precipitation rates and an increase in water vapor flux. In summary, the monthly variations in water vapor flux and budget indicate significant differences in moisture transport between the southwest and northeast monsoons. The upstream water vapor budget significantly affects the changes on stable water vapor isotopes, particularly $\delta^{18}\text{O}$. During the southwest monsoon, there is a clear increase in precipitation, with moisture transport primarily arriving from the northeast. During this period, evaporation in the upstream region exceeds precipitation, suggesting a higher water vapor content along the transport pathway, which corresponds to a continuous enrichment of $\delta^{18}\text{O}$ at Matara station. In contrast, during the northeast monsoon, moisture transport is mainly from the southwest. From December 2020 to January 2021, upstream precipitation exceeded evaporation, leading to a “washing effect” where water vapor continuously undergoes condensation and fractionation due to precipitation along the transport pathway, resulting in a gradual depletion of $\delta^{18}\text{O}$.



897

898 **Figure 8: Comparing average water vapor flux and water vapor budget during the (a)**
 899 **southwest monsoon and (b) northeast monsoon. The red dot indicates the location of Matara**
 900 **station.**

901

4.2 Comparing Main Features and Identifying Influencing Factors

902

During the both monsoon periods, specific humidity and stable water isotope composition showed a clear diurnal cycle at Matara station, primarily due to the significant contribution of local evapotranspiration to the overall moisture balance. In equatorial regions, seasonal variations in stable water vapor isotopes are largely governed by changes moisture sources and the transport processes. Ponmudi station, located in southern India (Lekshmy et al., 2018), shares many characteristics with Matara station, in that it is also a coastal city, influenced by both the southwest and northeast monsoons. During the summer, moisture sources for air arriving at Ponmudi are mostly located in the southern Arabian Sea and equatorial Indian Ocean, with relative humidity levels exceeding 70%. This high relative humidity, combined with a continuous supply of moisture from the Arabian Sea, results in significant rainfall in the Ponmudi region, exceeding 2040 mm.

914

Fluctuations of water vapor stable isotopes at shorter (weather) time scales are closely associated with regional convective activities. Research conducted on

916 precipitation and water vapor stable isotopes at Bangalore, another coastal city in
917 southern India, indicates that local meteorological parameters do not influence isotope
918 ratios (Rahul et al., 2016b). Rather, these ratios are affected by the integrated regional
919 convective activity, characterized by large-scale rainfall or outgoing longwave radiation
920 flux. Like Matara station, Bangalore is also affected by both the southwest and northeast
921 monsoons. The observed depletion in heavy isotopes may be due to the influx of
922 moisture from the Bay of Bengal, depleted due to the rainout effect, mixing with air
923 that has travelled overland crossing the Indian subcontinent.

924 Overall, the long-term monitoring of water vapor stable isotopes in South Asian
925 equatorial regions could highlight the importance of both seasonal and sub-seasonal
926 (weather-scale) variations, mostly due to changes in moisture sources and processes
927 that occur during the air mass transport at the circulation scale. Matara station served
928 as a good location to study the effects of moisture transport processes over the Indian
929 Ocean. We could also identify seasonal patterns that general agreement with previous
930 findings for tropical equatorial regions (Midhun et al., 2013; Rahul et al., 2016b;
931 Lekshmy et al., 2018).

932 933 **45. Summary and ~~conclusions~~Conclusions**

934 One-year (March 2020 to February 2021) in situ meteorological observations and
935 measurements of water vapor isotopic composition were conducted at Matara station,
936 Sri Lanka. Meteorological parameters exhibited diurnal variations during both
937 monsoon and non-monsoon periods. During the northeast monsoon, the diurnal
938 fluctuations in $\delta^{18}\text{O}$, temperature, and specific humidity are observed, with
939 maximum values reaching 1.1‰, 6.0°C, and 2.3 g/kg, respectively. In contrast, during
940 the southwest monsoon variations of these parameters exhibit only small magnitude
941 fluctuations of 0.45‰, 2.3°C, and 1.3 g/kg during the southwest monsoon period.
942 Atmospheric temperature affects isotopic composition through its effect on isotope
943 fractionation. Additionally, a weak seasonal variability in near-surface water vapor
944 isotopes is observed, with $\delta^{18}\text{O}$ typically showing high values (-11.1‰) during the

945 monsoon period and low values (-11.9‰) during the non-monsoon period. ~~The~~-d-
946 excess ~~exhibits exhibited the~~ lower value (12.7‰) during the monsoon period than ~~that~~
947 (~~14.7‰~~) during the non-monsoon period (~~14.7‰~~).

948 ~~The e~~Evaporation ~~from over~~ the northern Indian Ocean significantly impacts local
949 d-excess ~~at Matara~~. Contrary to previous research indicating a weak correlation ($r = -$
950 0.5) between d-excess in the Bay of Bengal and the sea surface relative humidity (RH_{SST})
951 (Midhun et al., 2013), ~~we found d-excess at Matara station exhibits a significantly a~~
952 ~~slightly stronger~~ negative correlation with ~~the~~ RH_{SST} during the monsoon periods, with
953 ~~the correlation values~~ of -0.61 and -0.62 ($p < 0.01$) ~~in for~~ the northern Indian Ocean and
954 ~~the~~ Bay of Bengal, respectively. This study underscores the capability of near-surface
955 d-excess to reflect the evaporation conditions over these oceanic ~~source~~ regions.

956 Consistent with previous research (Rahul et al., 2016b), large-scale rainfall and
957 regional convective activity (OLR) significantly impact isotope ratios at Matara station.
958 Notably, significant changes in $\delta^{18}\text{O}$ ~~are were~~ observed during a heavy rainfall event in
959 July 2020, with a sharp decline in isotopic values from -10.4‰ to -20.4‰ within 20
960 hours. During the southwest monsoon, strong cloud cover and high humidity over the
961 ocean may lead to $\delta^{18}\text{O}$ enrichment at ~~the~~ Matara station. The water vapor isotope
962 compositions observed during the southwest monsoon are similar as those observed in
963 the Bay of Bengal (Midhun et al., 2013). The deficiency of water vapor isotope values
964 at Matara station in autumn and winter is consistent with findings from other coastal
965 stations, such as Bangalore, Ponmudi, and Wayanad (Rahul et al., 2016b; Lekshmy et
966 al., 2018). Our ~~results study is the first to~~ pointed out that the correlation between OLR
967 and $\delta^{18}\text{O}$ peaks around 1-4 days, ~~which we~~ attributed to the impacts of cloud
968 distribution.

969 This study contributes to a better understanding of the ~~moisture~~ origins ~~of moisture~~
970 ~~arriving~~ at Matara station and ~~the~~ associated atmospheric transport. This ~~comprehensive~~
971 ~~dataset containing synchronous bined~~ water vapor isotope and meteorological ~~dataset~~
972 ~~measurements~~ offers extensive opportunities ~~to for~~ further ~~analysis analyses, e.g.,~~ of the
973 typical weather events, atmospheric patterns, and ocean-atmosphere interactions in the

974 equatorial region. ~~Ongoing~~ ~~Nevertheless, additional and continuous~~ observations of
975 water vapor stable isotopes in this region are ~~strongly urgently~~ needed ~~to be able to~~
976 ~~study. This will support studies on~~ interannual variability. Given the anticipated ~~changes~~
977 ~~in~~ numerous weather ~~and hydrological~~ processes ~~and hydrological changes~~ in equatorial
978 regions, future research should explore the impacts of typical weather events, and
979 ocean-atmosphere interactions, ~~to deepen~~ ~~ing~~ our understanding of extreme events and
980 large-scale atmospheric modes (e.g., ENSO, MJO, and IOD). Considering the temporal
981 and spatial variability in the ~~interaction dynamics~~ of tropical ocean-atmosphere systems,
982 high-resolution isotope model~~s or and~~ satellite ~~observation~~ datasets should be ~~employed~~
983 ~~combined~~ for a more comprehensive analysis in the future.

984 **Acknowledgements:**

985 This work was funded by The Second Tibetan Plateau Scientific Expedition and
986 Research (STEP) program (Grant No. 2019QZKK0208) and the National Natural
987 Science Foundation of China (Grants [41922002 and](#) 41988101-03 ~~and 41922002~~), as
988 well as the Innovation Program for Young Scholars of TPESER (QNCX2022ZD-01).
989 We thank staff in the China Sri Lanka Joint Center for Education and Research, Mr.
990 Charith Madusanka Widanage, and Dr. Di Dai for their invaluable support and
991 assistance with measurements.

992

993 **Author Contributions:**

994 **Yuqing Wu:** Data curation, Formal analysis, Writing - Original draft preparation.
995 **Jing Gao:** Data curation, Conceptualization, Methodology, Supervision, Writing -
996 Review and Editing, Funding acquisition. **Aibin Zhao:** Writing - Review and Editing,
997 Project administration. **Xiaowei Niu:** Data curation. **Yigang Liu:** Data curation. **Disna**
998 **Ratnasekera:** Project administration. **Tilak Priyadarshana Gamage:** Project
999 administration. **Amarasinghe Hewage Ruwan Samantha:** Data curation.

1000

1001 **Data availability:**

1002 The ERA5 dataset is the latest reanalysis dataset published by the European Centre
1003 for Medium-Range Weather Forecasts (ECMWF) (Hersbach et al., 2020)
1004 (<https://cds.climate.copernicus.eu/cdsapp#!/home>). The Global Data Assimilation
1005 System (GDAS) [has been](#) published by the US National Oceanic and Atmospheric
1006 Administration (NOAA) (<ftp://arlftp.arlhq.noaa.gov/archives/gdas1/>). The water vapor
1007 isotopic compositions dataset will be available on the Zenodo research data repository
1008 after manuscript publication.

1009

1010 **Competing interests:**

1011 The contact author has declared that none of the authors has any competing interests.

1012 **References**

1013 Aemisegger, F., Sturm, P., Graf, P., Sodemann, H., Pfahl, S., Knohl, A., and Wernli, H.:
1014 Measuring variations of $\delta^{18}\text{O}$ and $\delta^2\text{H}$ in atmospheric water vapour using two
1015 commercial laser-based spectrometers: an instrument characterisation study,
1016 *Atmos. Meas. Tech.*, 5, 1491-1511, <https://doi.org/10.5194/amt-5-1491-2012>,
1017 2012.

1018 Angert, A., Lee, J.E., and Yakir, D.: Seasonal variations in the isotopic composition of
1019 near-surface water vapour in the eastern Mediterranean, *Tellus B*, 60, 674-684,
1020 <https://doi.org/10.1111/j.1600-0889.2008.00357.x>, 2008.

1021 Bailey, A., Aemisegger, F., Villiger, L., Los, S.A., Reverdin, G., Quiñones Meléndez,
1022 E., Acquistapace, C., Baranowski, D.B., Böck, T., Bony, S., Bordsdorff, T.,
1023 Coffman, D., de Szoke, S.P., Diekmann, C.J., Dütsch, M., Ertl, B., Galewsky,
1024 J., Henze, D., Makuch, P., Noone, D., Quinn, P.K., Rösch, M., Schneider, A.,
1025 Schneider, M., Speich, S., Stevens, B., and Thompson, E.J.: Isotopic
1026 measurements in water vapor, precipitation, and seawater during EUREC4A,
1027 *Earth Syst. Sci. Data*, 15, 465-495, <https://doi.org/10.5194/essd-15-465-2023>,
1028 2023.

1029 Bandara, U., Agarwal, A., Srinivasan, G., Shanmugasundaram, J., and Jayawardena,
1030 I.M.S.: Intercomparison of gridded precipitation datasets for prospective
1031 hydrological applications in Sri Lanka, *Int. J. Climatol.*, 42, 3378-3396,
1032 <https://doi.org/10.1002/joc.7421>, 2022.

1033 Bavadekar, S.N., and Mooley, D.A.: Use of the equation of continuity of water vapour
1034 for computation of average precipitation over peninsular India during the
1035 summer monsoon, In: Lighthill, J., Pearce, P.R. (Eds.), *Monsoon Dynamics*,
1036 Cambridge University Press, Cambridge, pp., 261-268, 1981.

1037 Bedaso, Z., and Wu, S-Y.: Daily precipitation isotope variation in Midwestern United
1038 States: Implication for hydroclimate and moisture source, *Sci. Total Environ.*,
1039 713, 136631, <https://doi.org/10.1016/j.scitotenv.2020.136631>, 2020.

1040 Benetti, M., Aloisi, G., Reverdin, G., Risi, C., and Sèze, G.: Importance of boundary

1041 layer mixing for the isotopic composition of surface vapor over the subtropical
1042 North Atlantic Ocean, *J. Geophys. Res. Atmos.*, 120, 2190-2209,
1043 <https://doi.org/10.1002/2014JD021947>, 2015.

1044 Benetti, M., Lacour, J-L., Sveinbjörnsdóttir, A.E., Aloisi, G., Reverdin, G., Risi, C.,
1045 Peters, A.J., and Steen-Larsen, H.C.: A Framework to Study Mixing Processes
1046 in the Marine Boundary Layer Using Water Vapor Isotope Measurements,
1047 *Geophys. Res. Lett.*, 45(5), 2524-2532, <https://doi.org/10.1002/2018GL077167>,
1048 2018.

1049 Benetti, M., Reverdin, G., Pierre, C., Merlivat, L., Risi, C., Steen-Larsen, H.C., and
1050 Vimeux, F.: Deuterium excess in marine water vapor: Dependency on relative
1051 humidity and surface wind speed during evaporation, *J. Geophys. Res. Atmos.*,
1052 119, 584-593, <https://doi.org/10.1002/2013JD020535>, 2014.

1053 Bershaw, J., Penny, S.M., and Garzione, C.N.: Stable isotopes of modern water across
1054 the Himalaya and eastern Tibetan Plateau: Implications for estimates of
1055 paleoelevation and paleoclimate, *J. Geophys. Res. Atmos.*, 117, 110,
1056 <https://doi.org/10.1029/2011JD016132>, 2012.

1057 Bhattacharya, S., Pal, M., Panda, B., and Pradhan, M.: Spectroscopic investigation of
1058 hydrogen and triple-oxygen isotopes in atmospheric water vapor and
1059 precipitation during Indian monsoon season, *Isot. Environ. Health. S.*, 57, 368-
1060 385, <https://doi.org/10.1080/10256016.2021.1931169>, 2021.

1061 Bonne, J-L., Behrens, M., Meyer, H., Kipfstuhl, S., Rabe, B., Schönicke, L., Steen-
1062 Larsen, H.C., and Werner, M.: Resolving the controls of water vapour isotopes
1063 in the Atlantic sector, *Nat. Commun.*, 10, 1632, <https://doi.org/10.1038/s41467-019-09242-6>, 2019.

1065 Bonne, J-L., Masson-Delmotte, V., Cattani, O., Delmotte, M., Risi, C., Sodemann, H.,
1066 and Steen-Larsen, H.C.: The isotopic composition of water vapour and
1067 precipitation in Ivittuut, Southern Greenland, *Atmos. Chem. Phys.*, 14, 4419-
1068 2014, <https://doi.org/10.5194/acp-14-4419-2014>, 2014.

1069 Bonne, J-L., Meyer, H., Behrens, M., Boike, J., Kipfstuhl, S., Rabe, B., Schmidt, T.,

1070 Schönicke, L., Steen-Larsen, H.C., and Werner, M.: Moisture origin as a driver
1071 of temporal variabilities of the water vapour isotopic composition in the Lena
1072 River Delta, Siberia, *Atmos. Chem. Phys.*, 20, 10493-10511,
1073 <https://doi.org/10.5194/acp-20-10493-2020>, 2020.

1074 Bookhagen, B., and Burbank, D.W.: Toward a complete Himalayan hydrological
1075 budget: Spatiotemporal distribution of snowmelt and rainfall and their impact
1076 on river discharge, *J. Geophys. Res.*, 115, F03019,
1077 <https://doi.org/10.1029/2009JF001426>, 2010.

1078 Cai, Z., Tian, L., and Bowen, G.J.: ENSO variability reflected in precipitation oxygen
1079 isotopes across the Asian Summer Monsoon region, *Earth Planet. Sci. Lett.*, 475,
1080 25-33, <https://doi.org/10.1016/j.epsl.2017.06.035>, 2017.

1081 Cai, Z., and Tian, L.: Atmospheric Controls on Seasonal and Interannual Variations in
1082 the Precipitation Isotope in the East Asian Monsoon Region, *J. Climate*, 29,
1083 1339-1352, <https://doi.org/10.1175/JCLI-D-15-0363.1>, 2016.

1084 Chakraborty, S., Sinha, N., Chattopadhyay, R., Sengupta, S., Mohan, P.M., and Datye,
1085 A.: Atmospheric controls on the precipitation isotopes over the Andaman
1086 Islands, Bay of Bengal, *Sci. Rep.*, 6, 19555, <https://doi.org/10.1038/srep19555>,
1087 2016.

1088 Craig, H.: Isotopic Variation in Meteoric Waters. *Science*, 133, 1702-1703,
1089 <https://doi.org/10.1126/science.133.3465.1702>, 1961.

1090 Craig, H., and Gordon, L.I.: Deuterium and oxygen 18 variation in the ocean and the
1091 marine atmosphere, In: Tongiorgi, E. (Eds.), *Stable Isotopes in Oceanographic*
1092 *Studies and Paleotemperatures*, pp., 9-130, 1965.

1093 Curry, J.A., and Webster, P.J.: *Thermodynamics of Atmospheres and Oceans*, Academic
1094 Press, London, 31705, 1999.

1095 Dai, D., Gao, J., Steen-Larsen, H.C., Yao, T., Ma, Y., Zhu, M., and Li, S.: Continuous
1096 monitoring of the isotopic composition of surface water vapor at Lhasa,
1097 southern Tibetan Plateau, *Atmos. Res.*, 264, 105827,
1098 <https://doi.org/10.1016/j.atmosres.2021.105827>, 2021.

1099 Dansgaard, W.F.: Stable Isotopes in Precipitation, Tellus B, 16, 436-468,
1100 <https://doi.org/10.1111/j.2153-3490.1964.tb00181.x>, 1964.

1101 Delattre, H., Vallet-Couïn, C., and Sonzogni, C.: Deuterium excess in the
1102 atmospheric water vapour of a Mediterranean coastal wetland: regional vs. local
1103 signatures, *Atmos. Chem. Phys.*, 15, 10167-10181, <https://doi.org/10.5194/acp-15-10167-2015>, 2015.

1104 de Vries, A.J., Aemisegger, F., Pfahl, S., and Wernli, H.: Stable water isotope signals in
1105 tropical ice clouds in the West African monsoon simulated with a regional
1106 convection-permitting model, *Atmos. Chem. Phys.*, 22, 8863-8895,
1107 <https://doi.org/10.5194/acp-22-8863-2022>, 2022.

1108 Dhar, O., and Rakhecha, P.: Foreshadowing Northeast Monsoon Rainfall Over Tamil
1109 Nadu, *India, Mon. Weather Rev.*, 111, 109, [https://doi.org/10.1175/1520-0493\(1983\)111<0109:FNMROT>2.0.CO;2](https://doi.org/10.1175/1520-0493(1983)111<0109:FNMROT>2.0.CO;2), 1983.

1110 Diekmann, C.J., Schneider, M., Knippertz, P., de Vries, A.J., Pfahl, S., Aemisegger, F.,
1111 Dahinden, F., Ertl, B., Khosrawi, F., Wernli, H., and Braesicke, P.: A Lagrangian
1112 Perspective on Stable Water Isotopes During the West African Monsoon, *J.
1113 Geophys. Res. Atmos.*, 126, e2021JD034895,
1114 <https://doi.org/10.1029/2021JD034895>, 2021.

1115 <https://doi.org/10.1175/JHM-D-12-0107.1>, 2013.

1116 Dirmeyer, P.A., Jin, Y., Singh, B., and Yan, X.: Trends in Land–Atmosphere Interactions
1117 from CMIP5 Simulations, *J. Hydrometeorol.*, 14, 829-849,
1118 <https://doi.org/10.1175/JHM-D-12-0107.1>, 2013.

1119 Dütsch, M., Pfahl, S., Meyer, M., and Wernli, H.: Lagrangian process attribution of
1120 isotopic variations in near-surface water vapour in a 30-year regional climate
1121 simulation over Europe, *Atmos. Chem. Phys.*, 18, 1653-1669,
1122 <https://doi.org/10.5194/acp-18-1653-2018>, 2018.

1123 Gadgil, S.: The Indian Monsoon and Its Variability, *Rev. Earth Pl. Sci.*, 31, 429-467,
1124 <https://doi.org/10.1146/annurev.earth.31.100901.141251>, 2003.

1125 Galewsky, J., and Hurley, J.V.: An advection-condensation model for subtropical water
1126 vapor isotopic ratios, *J. Geophys. Res. Atmos.*, 115, 116,
1127

1128 <https://doi.org/10.1029/2009JD013651>, 2010.

1129 Galewsky, J., Steen-Larsen, H.C., Field, R.D., Worden, J., Risi, C., and Schneider, M.:
1130 Stable isotopes in atmospheric water vapor and applications to the hydrologic
1131 cycle, *Rev. Geophy.*, 54, 809-865, <https://doi.org/10.1002/2015RG000512>,
1132 2016.

1133 Gambheer, A.V., and Bhat, G.S.: Life Cycle Characteristics of Deep Cloud Systems
1134 over the Indian Region Using INSAT-1B Pixel Data, *Mon. Weather Rev.*, 128,
1135 4071-4083, [https://doi.org/10.1175/1520-0493\(2000\)129<4071:LCCODC>2.0.CO;2](https://doi.org/10.1175/1520-0493(2000)129<4071:LCCODC>2.0.CO;2), 2000.

1137 Gao, J., Masson-Delmotte, V., Risi, C., He, Y., and Yao, T.: What controls precipitation
1138 $\delta^{18}\text{O}$ in the southern Tibetan Plateau at seasonal and intra-seasonal scales? A
1139 case study at Lhasa and Nyalam, *Tellus B*, 65, 21043,
1140 <https://doi.org/10.3402/tellusb.v65i0.21043>, 2013.

1141 Gao, Y., Li, X., Leung, L. R., Chen, D., and Xu, J.: Aridity changes in the Tibetan
1142 Plateau in a warming climate, *Environ. Res. Lett.*, 9, 104013,
1143 <https://doi.org/10.1088/1748-9326/10/3/034013>, 2014.

1144 Gat, J.: Oxygen and hydrogen isotopes in the hydrologic cycle, *Annu. Rev. Earth Pl.
1145 Sci.*, 24, 225-262, <https://doi.org/10.1146/ANNUREV.EARTH.24.1.225>, 1996.

1146 Gedzelman, S., Lawrence, J., Gamache, J., Black, M., Hindman, E., Black, R., Dunion,
1147 J., Willoughby, H., and Zhang, X.: Probing hurricanes with stable isotopes of
1148 rain and water vapor, *Mon. Weather Rev.*, 131, 1112-1127,
1149 [https://doi.org/10.1175/1520-0493\(2003\)131<1112:Phwsio>2.0.Co;2](https://doi.org/10.1175/1520-0493(2003)131<1112:Phwsio>2.0.Co;2), 2003.

1150 Goff, J.A., and Gratch, S.: Low-pressure properties of water from -160°F to 212 °F.
1151 *Transactions of the American Society of Heating and Ventilating Engineers*, 52,
1152 95-122, 1946.

1153 Goswami, B.N., Venugopal, V., Sengupta, D., Madhusoodanan, M.S., and Xavier, P.K.:
1154 Increasing Trend of Extreme Rain Events Over India in a Warming Environment,
1155 *Science*, 314, 1442-1445, <https://doi.org/10.1126/science.1132027>, 2006.

1156 Graf, P., Wernli, H., Pfahl, S., and Sodemann, H.: A new interpretative framework for

1157 below-cloud effects on stable water isotopes in vapour and rain, *Atmos. Chem.*
1158 *Phys.*, 19, 747-765, <https://doi.org/10.5194/acp-19-747-2019>, 2019.

1159 Guo, X., Tian, L., Wen, R., Yu, W., and Qu, D.: Controls of precipitation $\delta^{18}\text{O}$ on the
1160 northwestern Tibetan Plateau: A case study at Ngari station, *Atmos. Res.*, 189,
1161 141-151, <https://doi.org/10.1016/j.atmosres.2017.02.004>, 2017.

1162 Hersbach, H., Bell, B., Berrisford, P., Hirahara, S., Horányi, A., Muñoz Sabater, J.,
1163 Nicolas, J., Peubey, C., Radu, R., Schepers, D., Simmons, A., Soci, C., Abdalla,
1164 S., Abellan, X., Balsamo, G., Bechtold, P., Biavati, G., Bidlot, J., Bonavita, M.,
1165 and Thépaut, J.N.: The ERA5 global reanalysis, *Q. J. Roy. Meteor. Soc.*,
1166 <https://doi.org/10.1002/qj.3803>, 2020.

1167 Hsu, Y-K., Holsen, T.M., and Hopke, P.K.: Comparison of hybrid receptor models to
1168 locate PCB sources in Chicago, *Atmos. Environ.*, 37, 545-562,
1169 [https://doi.org/10.1016/S1352-2310\(02\)00886-5](https://doi.org/10.1016/S1352-2310(02)00886-5), 2003.

1170 Jayasena, H.A.H., Chandrajith, R., and Dissanayake, C.B.: Spatial variation of isotope
1171 composition in precipitation in a tropical environment: a case study from the
1172 Deduru Oya river basin, Sri Lanka, *Hydrol. Process.*, 22, 4565-4570,
1173 <https://doi.org/10.1002/hyp.7060>, 2008.

1174 Kaushal, N., Breitenbach, S.F.M., Lechleitner, F.A., Sinha, A., Tewari, V.C., Ahmad,
1175 S.M., Berkelhammer, M., Band, S., Yadava, M., Ramesh, R., and Henderson,
1176 G.M.: The Indian Summer Monsoon from a Speleothem $\delta^{18}\text{O}$ Perspective-A
1177 Review, *Quaternary*, 1, 29, <https://doi.org/10.3390/quat1030029>, 2018.

1178 Kostrova, S.S., Meyer, H., Fernandoy, F., Werner, M., and Tarasov, P.E.: Moisture
1179 origin and stable isotope characteristics of precipitation in southeast Siberia,
1180 *Hydrol. Process.*, 34, 51-67, <https://doi.org/10.1002/hyp.13571>, 2020.

1181 Kurita, N.: Origin of Arctic water vapor during the ice-growth season, *Geophys. Res.*
1182 *Lett.*, 38, <https://doi.org/10.1029/2010GL046064>, 2011.

1183 Kurita, N.: Water isotopic variability in response to mesoscale convective system over
1184 the tropical ocean, *J. Geophys. Res. Atmos.*, 118, 10,376-10,390,
1185 <https://doi.org/10.1002/jgrd.50754>, 2013.

1186 Lekshmy, P.R., Midhun, M., and Ramesh, R.: Influence of stratiform clouds on δ D and
1187 $\delta^{18}\text{O}$ of monsoon water vapour and rain at two tropical coastal stations, *J.*
1188 *Hydrol.*, 563, 354-362, <https://doi.org/10.1016/j.jhydrol.2018.06.001>, 2018.

1189 Lekshmy, P.R., Midhun, M., and Ramesh, R.: Role of moisture transport from Western
1190 Pacific region on water vapor isotopes over the Bay of Bengal, *Atmos. Res.*,
1191 265, 105895, <https://doi.org/10.1016/j.atmosres.2021.105895>, 2022.

1192 Lekshmy, P.R., Midhun, M., Ramesh, R., and Jani, R.A.: ^{18}O depletion in monsoon rain
1193 relates to large scale organized convection rather than the amount of rainfall,
1194 *Sci. Rep.*, 4, 5661, <https://doi.org/10.1038/srep05661>, 2014.

1195 Li, L., and Garzione, C.N.: Spatial distribution and controlling factors of stable isotopes
1196 in meteoric waters on the Tibetan Plateau: Implications for paleoelevation
1197 reconstruction, *Earth Planet. Sci. Lett.*, 460, 302-314,
1198 <https://doi.org/10.1016/j.epsl.2016.11.046>, 2017.

1199 Liu, J., Ding, M., and Xiao, C.: Review on atmospheric water vapor isotopic
1200 observation and research: theory, method and modeling, *Prog. Geog.*, 34, 340-
1201 353, <https://doi.org/10.11820/dlkxjz.2015.03.009>, 2015.

1202 Liu, X., and Chen, B.: Climatic warming in the Tibetan Plateau during recent decades,
1203 *Int. J. Climatol.*, 20, 1729-1742, [https://doi.org/10.1002/1097-0088\(20001130\)20:14<1729::AID-JOC556>3.0.CO;2-Y](https://doi.org/10.1002/1097-0088(20001130)20:14<1729::AID-JOC556>3.0.CO;2-Y), 2000.

1205 Majoube, M.: Fractionnement en oxygène 18 entre la glace et la vapeur d'eau, *Journal
1206 De Chimie Physique*, 68, 625-636, 1971a.

1207 Majoube, M.: Fractionnement en oxygène 18 et en deutérium entre l'eau et sa vapeur,
1208 *Journal de Chimie Physique et de Physico Chimie Biologique*, 68, 1423-1436,
1209 <https://doi.org/10.1051/jcp/1971681423>, 1971b.

1210 Malmgren, B.A., Hulugalla, R., Hayashi, Y., and Mikami, T.: Precipitation trends in Sri
1211 Lanka since the 1870s and relationships to El Niño-southern oscillation, *Int. J.*
1212 *Climatol.*, 23, 1235-1252, <https://doi.org/10.1002/joc.921>, 2003.

1213 Masunaga, H., and Kummerow, C.: Observations of tropical precipitating clouds
1214 ranging from shallow to deep convective systems, *Geophys. Res. Lett.*, 33, 805,

1215 <https://doi.org/10.1029/2006GL026547>, 2006.

1216 Merlivat, L., and Jouzel, J.: Global climatic interpretation of the deuterium-oxygen 18
1217 relationship for precipitation, *J. Geophys. Res. Oceans.*, 84, 5029-5033.

1218 <https://doi.org/10.1029/JC084iC08p05029>, 1979.

1219 Midhun, M., Lekshmy, P.R., and Ramesh, R.: Hydrogen and oxygen isotopic
1220 compositions of water vapor over the Bay of Bengal during monsoon, *Geophys.*
1221 *Res. Lett.*, 40, 6324-6328, <https://doi.org/10.1002/2013GL058181>, 2013.

1222 Ohring, G., Gruber, A., and Ellingson, R.: Satellite Determinations of the Relationship
1223 between Total Longwave Radiation Flux and Infrared Window Radiance, *J.*
1224 *Appl. Meteorol. Clim.*, 23, 416-425, [https://doi.org/10.1175/1520-0450\(1984\)023<0416:SDOTRB>2.0.CO;2](https://doi.org/10.1175/1520-0450(1984)023<0416:SDOTRB>2.0.CO;2), 1984.

1225 Pang, Z., Kong, Y., Froehlich, K., Huang, T., Yuan, L., Li, Z., and Wang, F.: Processes
1226 affecting isotopes in precipitation of an arid region, *Tellus B*, 63, 352-359,
1227 <https://doi.org/10.1111/j.1600-0889.2011.00532.x>, 2011.

1228 Permana, D.S., Thompson, L.G., and Setyadi, G.: Tropical West Pacific moisture
1229 dynamics and climate controls on rainfall isotopic ratios in southern Papua,
1230 Indonesia, *J. Geophys. Res. Atmos.*, 121, 2222-2245,
1231 <https://doi.org/10.1002/2015JD023893>, 2016.

1232 Pfahl, S., and Wernli, H.: Lagrangian simulations of stable isotopes in water vapor: An
1233 evaluation of nonequilibrium fractionation in the Craig-Gordon model, *J.*
1234 *Geophys. Res. Atmos.*, 114, 108, <https://doi.org/10.1029/2009JD012054>, 2009.

1235 Rahul, P., Ghosh, P., and Bhattacharya, S.K.: Rainouts over the Arabian Sea and
1236 Western Ghats during moisture advection and recycling explain the isotopic
1237 composition of Bangalore summer rains, *J. Geophys. Res. Atmos.*, 121, 6148-
1238 6163, <https://doi.org/10.1002/2015JD024579>, 2016a.

1239 Rahul, P., Ghosh, P., Bhattacharya, S.K., and Yoshimura, K.: Controlling factors of
1240 rainwater and water vapor isotopes at Bangalore, India: Constraints from
1241 observations in 2013 Indian monsoon, *J. Geophys. Res. Atmos.*, 121, 13,936-
1242 13,952, <https://doi.org/10.1002/2016JD025352>, 2016b.

1243

1244 Ranjan, S., Al, R., Keesari, T., Singh, V., Kumar, P., and Manish Leuenberger, M.: Triple
1245 Water Vapour-Isotopologues Record from Chhota Shigri, Western Himalaya,
1246 India: A Unified Interpretation based on $\delta^{17}\text{O}$, $\delta^{18}\text{O}$, δD and Comparison to
1247 Meteorological Parameters, *Front. Earth Sci.*, 8, 599-632,
1248 <https://doi.org/10.3389/feart.2020.599632>, 2021.

1249 Ravisankar, L., Madhavan, M., and Ramesh, R.: Spatial variation of amount effect over
1250 peninsular India and Sri Lanka: Role of seasonality, *Geophys. Res. Lett.*, 42,
1251 5500-5507, <https://doi.org/10.1002/2015GL064517>, 2015.

1252 Risi, C., Bony, S., and Vimeux, F.: Influence of convective processes on the isotopic
1253 composition ($\delta^{18}\text{O}$ and δD) of precipitation and water vapor in the tropics: 2.
1254 Physical interpretation of the amount effect, *J. Geophys. Res. Atmos.*, 113, 306,
1255 <https://doi.org/10.1029/2008JD009943>, 2008.

1256 Salamalikis, V., Argiriou, A.A., and Dotsika, E.: Stable isotopic composition of
1257 atmospheric water vapor in Patras, Greece: A concentration weighted trajectory
1258 approach, *Atmos. Res.*, 152, 93-104,
1259 <https://doi.org/10.1016/j.atmosres.2014.02.021>, 2015.

1260 Saranya, P., Krishan, G., Rao, M.S., Kumar, S., and Kumar, B.: Controls on water vapor
1261 isotopes over Roorkee, India: Impact of convective activities and depression
1262 systems, *J. Hydrol.*, 557, 679-687,
1263 <https://doi.org/10.1016/j.jhydrol.2017.12.061>, 2018.

1264 Schumacher, C.: Shallow tropical convection: How often does it rain? *Bull. Am.
1265 Meteorol. Soc.*, 87, 23-25, 2006.

1266 Singh, P., and Bengtsson, L.: Hydrological sensitivity of a large Himalayan basin to
1267 climate change, *Hydrol. Process.*, 18, 2363-2385,
1268 <https://doi.org/10.1002/hyp.1468>, 2004.

1269 Srivastava, R., Ramesh, R., Gandhi, N., Jani, R.A., and Singh, A.K.: Monsoon onset
1270 signal in the stable oxygen and hydrogen isotope ratios of monsoon vapor,
1271 *Atmos. Environ.*, 108, 117-124,
1272 <https://doi.org/10.1016/j.atmosenv.2015.02.062>, 2015.

1273 Steen-Larsen, H.C., Masson-Delmotte, V., Hirabayashi, M., Winkler, R., Satow, K.,
1274 Prié, F., Bayou, N., Brun, E., Cuffey, K., Dahl-Jensen, D., Dumont, M.,
1275 Guillevic, M., Kipfstuhl, J., Landais, A., Popp, T., Risi, C., Steffen, K., Stenni,
1276 B., and Sveinbjörnsdóttir, A.: What controls the isotopic composition of
1277 Greenland surface snow? *Clim. Past.*, 10, 379-392, <https://doi.org/10.5194/cpd-9-6035-2013>, 2013a.

1279 Steen-Larsen, H.C., Johnsen, S.J., Masson-Delmotte, V., Stenni, B., Risi, C., Sodemann,
1280 H., Balslev-Clausen, D., Blunier, T., Dahl-Jensen, D., Ellehøj, M.D., Falourd,
1281 S., Grindsted, A., Gkinis, V., Jouzel, J., Popp, T., Sheldon, S., Simonsen, S.B.,
1282 Sjolte, J., Steffensen, J.P., Sperlich, P., Sveinbjörnsdóttir, A.E., Vinther, B.M.,
1283 and White, J.W.C.: Continuous monitoring of summer surface water vapor
1284 isotopic composition above the Greenland Ice Sheet, *Atmos. Chem. Phys.*, 13,
1285 4815-4828, <https://doi.org/10.5194/acp-13-4815-2013>, 2013b.

1286 Steen-Larsen, H.C., Sveinbjörnsdóttir, A.E., Jonsson, T., Ritter, F., Bonne, J-L.,
1287 Masson-Delmotte, V., Sodemann, H., Blunier, T., Dahl-Jensen, D., and Vinther,
1288 B.M.: Moisture sources and synoptic to seasonal variability of North Atlantic
1289 water vapor isotopic composition, *J. Geophys. Res. Atmos.*, 120, 5757-5774,
1290 <https://doi.org/10.1002/2015JD023234>, 2015.

1291 Stewart, M.K.: Stable isotope fractionation due to evaporation and isotopic exchange
1292 of falling waterdrops: Applications to atmospheric processes and evaporation of
1293 lakes, *J. Geophys. Res.*, 80, 1133-1146,
1294 <https://doi.org/10.1029/JC080i009p01133>, 1975.

1295 Sturm, P., and Knohl, A.: Water vapor $\delta^2\text{H}$ and $\delta^{18}\text{O}$ measurements using off-axis
1296 integrated cavity output spectroscopy, *Atmos. Meas. Tech.*, 3, 67-77,
1297 <https://doi.org/10.5194/amt-3-67-2010>, 2010.

1298 Thompson, L.G., Davis, M.E., Mosley-Thompson, E., Beaudon, E., Porter, S.E.,
1299 Kutuzov, S., Lin, P.N., Mikhaleko, V.N., and Mountain, K.R.: Impacts of
1300 Recent Warming and the 2015/2016 El Niño on Tropical Peruvian Ice Fields, *J.*
1301 *Geophys. Res. Atmos.*, 122, 12,688-12,701,

1302 <https://doi.org/10.1002/2017JD026592>, 2017.

1303 Tremoy, G., Vimeux, F., Mayaki, S., Souley, I., Cattani, O., Risi, C., Favreau, G., and
1304 Oi, M.: A 1-year long $\delta^{18}\text{O}$ record of water vapor in Niamey (Niger) reveals
1305 insightful atmospheric processes at different timescales, *Geophys. Res. Lett.*,
1306 39(8), 805, <https://doi.org/10.1029/2012GL051298>, 2012.

1307 Uemura, R., Matsui, Y., Yoshimura, K., Motoyam, H., and Yoshida, N.: Evidence of
1308 deuterium excess in water vapor as an indicator of ocean surface conditions, *J.*
1309 *Geophys. Res. Atmos.*, 113, D19114, <https://doi.org/10.1029/2008JD010209>,
1310 2008.

1311 Villiger, L., and Aemisegger, F.: Water isotopic characterisation of the cloud–circulation
1312 coupling in the North Atlantic trades – Part 2: The imprint of the atmospheric
1313 circulation at different scales, *Atmos. Chem. Phys.*, 24, 957-976,
1314 <https://doi.org/10.5194/acp-24-957-2024>, 2024.

1315 Vimeux, F., Tremoy, G., Risi, C., and Gallaire, R.: A strong control of the South
1316 American SeeSaw on the intra-seasonal variability of the isotopic composition
1317 of precipitation in the Bolivian Andes, *Earth. Planet. Sci. Lett.*, 307, 47-58,
1318 <https://doi.org/10.1016/j.epsl.2011.04.031>, 2011.

1319 Wallace, J.M., and Hobbs, P.V.: 3-Atmospheric Thermodynamics, *Atmos. Sci.*, 63-111,
1320 <https://doi.org/10.1016/B978-0-12-732951-2.50008-9>, 2006.

1321 Wang, B.: The Asian monsoon. Springer praxis books, Springer/Praxis Publishing Co,
1322 Berlin, 787 pp., 651-683, 2006.

1323 Webster, P.J., Magana, V.O., Palmer, T.N., Shukla, J., Tomas, R.A., Yanai, M., and
1324 Yasunari, T.: Monsoons: Processes, predictability, and the prospects for
1325 prediction, *J. Geophys. Res. Oceans.*, 103, 14451-14510,
1326 <https://doi.org/10.1029/97JC02719>, 1998.

1327 Worden, J., Noone, D., Bowman, K., Beer, R., Eldering, A., Fisher, B., Gunson, M.,
1328 Goldman, A., Herman, R., Kulawik, S., Lampel, M., Osterman, G., Rinsland,
1329 C., Rodgers, C., Sander, S., Shephard, M., Webster, C., and Worden, H.:
1330 Importance of rain evaporation and continental convection in the tropical water

1331 cycle, *Nature*, 445, 528-532, <https://doi.org/10.1038/nature05508>, 2007. Xu, T.,
1332 Pang, H., Zhan, Z., Zhang, W., Guo, H., Wu, S., and Hou, S.: Water vapor
1333 isotopes indicating rapid shift among multiple moisture sources for the 2018-
1334 2019 winter extreme precipitation events in southeastern China, *Hydrol. Earth
1335 Syst. Sci.*, 26, 117-127, <https://doi.org/10.5194/hess-26-117-2022>, 2022.

1336 Yao, T., Thompson, L.G., Mosbrugger, V., Zhang, F., Ma, Y., Luo, T., Xu, B., Yang, X.,
1337 Joswiak, D.R., Wang, W., Joswiak, M.E., Devkota, L.P., Tayal, S., Jilani, R., and
1338 Chen, F.: Third Pole Environment (TPE), *Environ. Dev.*, 7, 52-64,
1339 <https://doi.org/10.1016/j.envdev.2012.04.002>, 2012.